

# The Structure of Aconitase

A.H. Robbins and C.D. Stout

Research Institute of Scripps Clinic, 10666 North Torrey Pines Road, La Jolla, California 92037

**ABSTRACT** The crystal structure of the 80,000 Da Fe–S enzyme aconitase has been solved and refined at 2.1 Å resolution. The protein contains four domains; the first three from the N-terminus are closely associated around the [3Fe–4S] cluster with all three cysteine ligands to the cluster being provided by the third domain. Association of the larger C-terminal domain with the first three domains creates an extensive cleft leading to the Fe–S cluster. Residues from all four domains contribute to the active site region, which is defined by the Fe–S cluster and a bound  $\text{SO}_4^{2-}$  ion. This region of the structure contains 4 Arg, 3 His, 3 Ser, 2 Asp, 1 Glu, 3 Asn, and 1 Gln residues, as well as several bound water molecules. Three of these side chains reside on a three-turn  $3_{10}$  helix in the first domain. The  $\text{SO}_4^{2-}$  ion is bound 9.3 Å from the center of the [3Fe–4S] cluster by the side chains of 2 Arg and 1 Gln residues. Each of 3 His side chains in the putative active site is paired with Asp or Glu side chains.

**Key words:** aconitase, iron–sulfur enzyme, crystal structure

## INTRODUCTION

Aconitase employs an iron–sulfur cluster to catalyze a stereospecific dehydration/rehydration reaction. The reaction is the conversion of citrate to isocitrate via *cis*-aconitate in the second and third steps of the tricarboxylic acid cycle. Ogston<sup>1</sup> proposed that an enzyme surface must have three points of contact with a substrate such as citrate<sup>2</sup> in order to discriminate between chemically equivalent moieties. The aconitase reaction requires that a base on the enzyme abstract a proton from either isocitrate or citrate and reprotonate *cis*-aconitate with concomitant exchange of the hydroxyl with water from solvent.<sup>3–6</sup> Subsequent to the discovery that iron was required for activity,<sup>7,8</sup> a mechanism was proposed based on crystal structures of inorganic complexes of aconitase substrates and the idea that three coordination sites of octahedral iron could coordinate *cis*-aconitate in either of two conformations while promoting nucleophilic attack by coordinated water or hydroxyl.<sup>9–11</sup>

The iron in aconitase is present within a Fe–S cluster.<sup>12,13</sup> The nature of this cluster in the beef heart mitochondrial protein has been shown to be a

[3Fe–4S] cluster with cubane-like geometry in the inactive form of the enzyme,<sup>14–16</sup> which upon activation readily converts to a [4Fe–4S] cluster.<sup>17–20</sup> Mössbauer experiments demonstrate that the added fourth Fe becomes spectroscopically distinct upon binding of substrates.<sup>21,22</sup> Electron nuclear double resonance and Mössbauer studies using <sup>17</sup>O-labeled substrates and inhibitors support a mechanism in which the Fe–S cluster simultaneously binds a hydroxyl of substrate or derived from substrate, one carboxyl of substrate, and a water molecule.<sup>23–25</sup> Kinetic experiments show the rate-limiting step to be pH-independent release and rebinding of *cis*-aconitate, the intermediate product.<sup>26</sup> The stereospecificity of the reaction is explained by 180° rotation of *cis*-aconitate upon rebinding.<sup>25</sup> Based on the binding of nitro-analogs the transition state to *cis*-aconitate from citrate or isocitrate is a carbanion.<sup>27</sup> The hydration reactions of carboxy alkenes coordinated to metal ions<sup>28,29</sup> are consistent with the proposed mechanism.<sup>25</sup>

Beef heart mitochondrial aconitase [EC 4.2.1.3] is a single polypeptide chain of  $M_r$  80,000; as aerobically isolated the enzyme contains a [3Fe–4S] cluster.<sup>15</sup> The amino acid sequences of eight cysteinyl-tryptic peptides derived from beef heart aconitase comprise 196 residues of the entire sequence.<sup>30</sup> A primary sequence of 755 residues of the pig heart mitochondrial enzyme from the C-terminus has been determined from the DNA sequence.<sup>31</sup> The sequences of a number of tryptic and cyanogen bromide peptides derived from pig heart aconitase have been aligned with respect to the DNA sequence.<sup>32</sup> The homology of the beef heart cysteine peptide sequences with the pig heart DNA-derived sequence is greater than 98%.<sup>30,31</sup> The N-terminus of the mature enzyme is blocked;<sup>30,32</sup> the identity of this residue and the site of proteolysis of the putative leader peptide are unknown.

The aconitase reaction involves direct participation of an Fe–S cluster in an enzymatic process in which there is no net oxidation or reduction of substrate. In this paper we present the refined 2.1 Å

Received October 21, 1988; revision accepted April 26, 1989.

Address reprint requests to C.D. Stout, Research Institute of Scripps Clinic, 10666 North Torrey Pines Road, La Jolla, CA 92037.

resolution structure of pig heart mitochondrial aconitase crystallized in the inactive [3Fe-4S] cluster form. The structure provides a framework in which to begin to correlate the extensive kinetic and spectroscopic data on the enzyme. Previously it was shown from analysis of the anomalous difference Patterson map that the [3Fe-4S] cluster has Fe-Fe separations less than 3.0 Å,<sup>33</sup> consistent with the EXAFS data.<sup>14</sup> The inactive structure of aconitase has been used as a basis for determining the structure of the activated enzyme at 2.5 Å resolution.<sup>34</sup> The activated state in the crystal contains a [4Fe-4S] cluster and is isomorphous with the inactive structure reported here.

## EXPERIMENTAL PROCEDURES

### Crystals

Pig heart aconitase was prepared and single crystals were grown as previously described.<sup>35</sup> The space group is  $P2_12_12$  with  $a = 173.6$  Å,  $b = 72.0$  Å,  $c = 72.7$  Å, one molecule per asymmetric unit and a solvent content of 57% by volume. Dissolved crystals of the inactive enzyme yield a Fe:S ratio of 3:4, consistent with the presence of a [3Fe-4S] cluster, and when activated have a specific activity comparable to purified beef enzyme.<sup>14,33</sup>

The standard crystallization procedure uses 15 mM tricarballoylate as the inhibitor. However, in the course of derivative screening, we also surveyed crystallization conditions using 15 mM *trans*-aconitate, citrate, *cis*-aconitate, isocitrate, oxalic, malic, maleic, succinate, glutaric, and glutaric acids as the inhibitor. With the exception of *trans*-aconitate, the presence of any one of the compounds yielded diamond-shaped orthorhombic crystals as normally observed in the standard seeding procedure. The only compound tested which failed to yield crystals was mercaptosuccinic acid (thiomalate). If no di- or tricarboxylic acid was present, the protein denatured and precipitated. Crystals grown in the presence of *trans*-aconitate exhibited a different habit, being blocks elongated on  $b$  ( $0.3 \times 0.7 \times 0.3$  mm) rather than diamonds elongated on  $a$  ( $1.0 \times 0.5 \times 0.3$  mm), even though the seed crystals were small tricarballoylate-grown diamonds. The similar results obtained with the different compounds are consistent with the presence of a bound sulfate in the active site, rather than one of the inhibitors, as subsequently determined.

The diffraction patterns of the crystals with any of the inhibitors present were isomorphous with the native, tricarballoylate-grown crystals. Although also isomorphous, the *trans*-aconitate-grown crystals displayed temperature-dependent nucleation unique to this inhibitor. Crystals grown at 22–23°C were orthorhombic, but crystals grown at 18°C were monoclinic and twinned. The twin plane is normal to  $c$ ; the monoclinic cells have very close to one-half the

$a$  axis length such that the 2-fold axis parallel to  $c$  in  $P2_12_12$  is preserved. This gives rise to nonintegrally spaced reflections along  $a^*$ . This twinning phenomenon does not appear to be directly related to pseudo-tetragonal twinning previously observed in which  $b = c$ .<sup>35</sup> For the single orthorhombic form, native crystals were soaked and mounted at ambient temperature in a synthetic mother liquor of 2.9 M  $(\text{NH}_4)_2\text{SO}_4$ , 0.35 NaCl, and 0.25 M bis-Tris buffer at pH 7.0. Under these conditions doubling of the  $c$  axis, another unit cell transformation observed previously, in Tris-HCl buffer, pH 7.0, at 4°C,<sup>33</sup> does not occur.

### Derivatives

A large number of compounds were screened in an effort to make isomorphous derivatives of the single orthorhombic crystals. While the crystals are quite robust, the protein is either labile to heavy atom reagents, or inert to less reactive compounds and ions. However, two isomorphous derivatives were prepared, with platinum and mercury, and a third derivative was made by removing Fe from native crystals.

In all of the screening experiments the inhibitor present in the native crystals had no effect on the reproducibility of intensity changes. Soaked crystals were evaluated by precession or oscillation photography. The Pt derivative is made by soaking crystals in a freshly prepared solution of 10 mM  $\text{K}_2\text{PtCl}_4$  in synthetic mother liquor in the dark for 3 days. Initially this derivative was prepared at pH 8.5, in an effort to promote reactivity of basic residues. However, the native diffraction pattern exhibits nonisomorphous intensity changes at pH 8.5 vs. 7.0, which is perhaps related to the transition to the linear [3Fe-4S] cluster form of the enzyme at pH 9.5.<sup>36</sup> At pH 7.0 the intensity differences are isomorphous. The Hg derivative was prepared by soaking crystals for 4 days in synthetic mother liquor containing 0.10 mM *p*-hydroxymercuribenzoic acid sulfonate (PHMBS). For both Pt and Hg soaked crystals, the crystals were washed and back-soaked for 1 day in fresh synthetic mother liquor prior to mounting and data collection. The apoprotein derivative was prepared by back-soaking the native crystals against a large volume (1.0 ml) of synthetic mother liquor. After 6–8 weeks the crystals became bleached and colorless, but otherwise unchanged. The bleaching behavior was variable for different native crystals. Addition of 10  $\mu\text{M}$  EDTA did not significantly accelerate the bleaching of the crystals.

### Data Collection

A summary of aconitase data sets is given in Table I. Data were collected by oscillation photography and on two area detector instruments. All of the crystals contained tricarballoylate as the inhibitor, with the exception of the Pt and Hg data collection

TABLE I. Data Collection and Multiple Isomorphous Replacement

Data set	Number of crystals	Data collection crystals				Rdiff(F) <sup>‡</sup>
		Total reflections	Independent reflections	Resolution (Å)	Rsymm(I) <sup>†</sup>	
Film						
Native*	18	144,602	24,343	2.7	0.074 <sup>§</sup>	
Apo	1	36,111	15,879	3.0	0.108	0.147
Area detector (multiwire)						
Native	3	149,730	21,718	3.0	0.058 <sup>§</sup>	
Apo	1	67,553	17,929	3.0	0.041	0.128
Hg	1	77,440	18,960	3.0	0.039 <sup>§</sup>	0.094
Pt	1	61,152	11,924	3.5	0.060	0.152
Area detector (Xentronics)						
Native	3	350,360	47,583	2.1	0.106	
Heavy atom parameters for 3.0 Å MIR map						
Site	Relative Occupancy	x	y	z	B (Å <sup>2</sup> )	
<Fe> <sup>**</sup>	0.0310	0.1629	0.0134	0.3597	42	
<Fe> <sup>††</sup>	0.0093	0.1682	0.0104	0.3651	24	
Hg1 <sup>‡‡</sup>	0.0194	0.4846	0.3006	0.5109	36	
Hg2	0.0094	0.1860	0.0251	0.0470	35	
Pt1 <sup>‡‡</sup>	0.0154	0.0666	0.4650	0.4969	34	
Pt2	0.0079	0.4834	0.2871	0.5772	38	
Pt3	0.0081	0.2879	0.1609	0.3428	50	
Pt4	0.0115	0.0215	0.1391	0.5249	57	
Pt5	0.0071	0.4361	-0.0052	0.4821	30	
Pt6	0.0059	0.3561	0.3823	0.1323	38	
Pt7	0.0073	0.4195	0.1305	0.6696	31	

\*Reference 33.

<sup>†</sup> $R = \sum_h \sum_i |I_i - \bar{I}| / \sum_h \sum_i \bar{I}$  where  $\bar{I}$  is the mean intensity of the  $i$  observations of reflection  $h$ .<sup>‡</sup> $R = \sum_h | |F_{pH}| - |F_p| | / \sum_h |F_p|$  where  $|F_{pH}|$  and  $|F_p|$  are the derivative and native structure amplitudes, respectively.<sup>§</sup>Rsymm (I) in point group 222 for film native 0.070, for area detector (multiwire) native data 0.043, and for Hg data 0.029.<sup>\*\*</sup>One site refinement against native anomalous data at 4.0 Å.<sup>††</sup>One site refinement against apo derivative isomorphous data at 3.5 Å.<sup>‡‡</sup>Heavy atom refinement against isomorphous difference data at 3.5 Å for Hg derivative and at 4.5 Å for Pt derivative.

crystals which had *trans*-aconitate and glutaric acid, respectively, as the inhibitors present. Film data were collected by oscillation photography as previously described for the native data set which includes the Fe anomalous scattering signal.<sup>33</sup> The apo derivative film data set was collected on a single crystal mounted on  $\alpha$  and translated twice along the spindle axis to expose different regions of the crystal and to minimize decay. The crystal was rotated through 90° with 2° oscillations per cassette. The data were collected on a GX-20 rotating anode X-ray generator operated at 40 kV, 40 mA with Ni-filtered CuK $\alpha$  radiation (0.2 mm collimator, crystal to film distance 10 cm). The data were digitized on a 100  $\mu$ m raster using an Optronics P-1000 film scanner and indexed and integrated as for the native data set. A partial film data set to 3.0 Å resolution for Hg-soaked crystals with *trans*-aconitate as inhibitor present was also collected and processed in order to evaluate the derivative.

Area detector data were collected at the UCSD multiwire diffractometer facility.<sup>37–39</sup> The data collection strategy followed that of Xuong<sup>37</sup> for two de-

tectors with  $\theta_c = \pm 23^\circ$  for high-resolution data, followed by  $\theta_c = +7, -11^\circ$  for low-resolution data. For the native data additional runs were collected at  $-\chi$ ,  $\phi + 180^\circ$  to increase redundancy in measurement of Bijvoet pairs. The crystal to detector distance was 100–110 cm; the X-ray generator was operated at 40 kV, 50 mA for monochromatized CuK $\alpha$  radiation. Total exposure time per crystal was 2 days. Frames were collected in  $\omega$  steps of 0.08°–0.16° with exposure times of 20–40 seconds depending upon resolution and crystal mosaicity. Data were reduced, edited, and scaled in point group *mmm*, and scale factors applied to the Bijvoet pair data for native and Hg data sets.<sup>39</sup>  $\langle I \rangle / \langle \sigma(I) \rangle$  over all resolution ranges for the four data sets ranged from 12.9 to 16.1; for data in the range 3.03–3.00 Å  $\langle I \rangle / \langle \sigma(I) \rangle$  ranged from 6.7 to 9.2.

Xentronics area detector data were collected with a rotating anode X-ray generator (Ni-filtered CuK $\alpha$  radiation, 0.2 mm focal spot). The detector was placed 22 cm from the crystal and equipped with a helium chamber. The data were collected at  $\chi$  of 45° and 2 $\theta$  setting angles of 30° and 14° in ranges of  $\omega$

TABLE II. 2.1 Å Resolution Native Data and Refinement

Data Collection and Scaling				
Xentronics Data				
Resolution range	Independent reflections		Percent $\leq 0.0\sigma_F$	Average $I/\sigma(I)$
	Number observed	Number possible		
$\infty$ –3.74	10,097	10,181	99.2	24.4
3.74–2.97	9,484	9,801	96.8	16.2
2.97–2.59	8,975	9,731	92.6	9.1
2.59–2.35	8,375	9,688	86.4	5.7
2.35–2.19	7,376	9,641	76.5	3.9
2.19–2.06	3,276	9,635	34.0	2.7
Total	47,583	58,677	81.1	15.2
Scaling				
Data set	Total reflections	Independent reflections	Common reflections*	Rmerge on $ F ^\dagger$
Film	144,602	24,343	23,495	0.084
Multiwire	149,730	21,718	21,047	0.084
Xentronics	350,360	47,583		
Merged	644,692	48,231		
R-factor for the Aconitase Structure				
Resolution range (Å)	Number of reflections <sup>†</sup>		R-factor <sup>‡</sup>	
2.06–2.15	2059		0.288	
2.15–2.25	4464		0.302	
2.25–2.38	5249		0.286	
2.38–2.54	5630		0.266	
2.54–2.75	5906		0.252	
2.75–3.07	6519		0.209	
3.07–3.61	6700		0.178	
3.61–5.00	6761		0.148	
Total	43,288		0.209	
$F_{\text{obs}}$ –amplitude range	Number of reflections <sup>†</sup>		R-factor <sup>‡</sup>	
0.08–13.28	25,457		0.319	
13.28–26.48	13,170		0.184	
26.48–39.68	3,399		0.137	
39.68–52.88	963		0.092	
52.88–66.07	239		0.067	
66.07–79.27	43		0.067	
79.27–92.47	12		0.067	
92.47–105.70	5		0.042	
Total	43,288		0.209	

\*Film and multiwire data scaled to Xentronics data and averaged.

<sup>†</sup>Includes all observed data in the merged data set  $\geq 0.0\sigma_F$ .

<sup>‡</sup> $R = \sum_h | |F_o| - |F_c| | / \sum_h |F_o|$  where  $|F_o|$  and  $|F_c|$  are observed and calculated structure amplitudes, respectively.

( $\pm 30$ ) with steps of  $0.20^\circ$  on  $\omega$ . Ten ranges of  $\omega$  (runs) were collected from each of three crystals. Individual frames were counted for 5 minutes at  $2\theta$  of  $30^\circ$  and 2.5 minutes at  $2\theta$  of  $14^\circ$ . The total data collection time was 8 days per crystal. Following collection of each  $2\theta$   $14^\circ$  run, the crystal was rotated  $23^\circ$  on  $\phi$  (one-fourth of the  $90^\circ$  asymmetric unit) and translated in the beam to a fresh, unexposed region of the crystal. In this way serious decay effects were avoided and on average 7-fold redundancy was achieved in the observations (Table I). The reflection data were integrated, reduced, merged, and scaled.<sup>39</sup> The completeness of the Xentronics area detector native data set to 2.1 Å resolution is summarized in Table II. The film and multiwire area

detector native data sets were scaled to the 2.1 Å native data using anisotropic shape factors in shells of  $\sin \theta/\lambda$ . The scaled data sets were then merged and averaged (Table II) to yield a single native data set for phase extension and refinement calculations. For isomorphous replacement calculations the multiwire and film data sets were used independently.

### MIR Calculations

The film native anomalous data (Table I) were used as a basis for initiating phase calculations for the protein. The native anomalous scattering film data to 2.7 Å resolution had been used to locate the Fe–S cluster in the unit cell; analysis of the Fe–Fe vectors confirmed that the Fe–Fe separations are

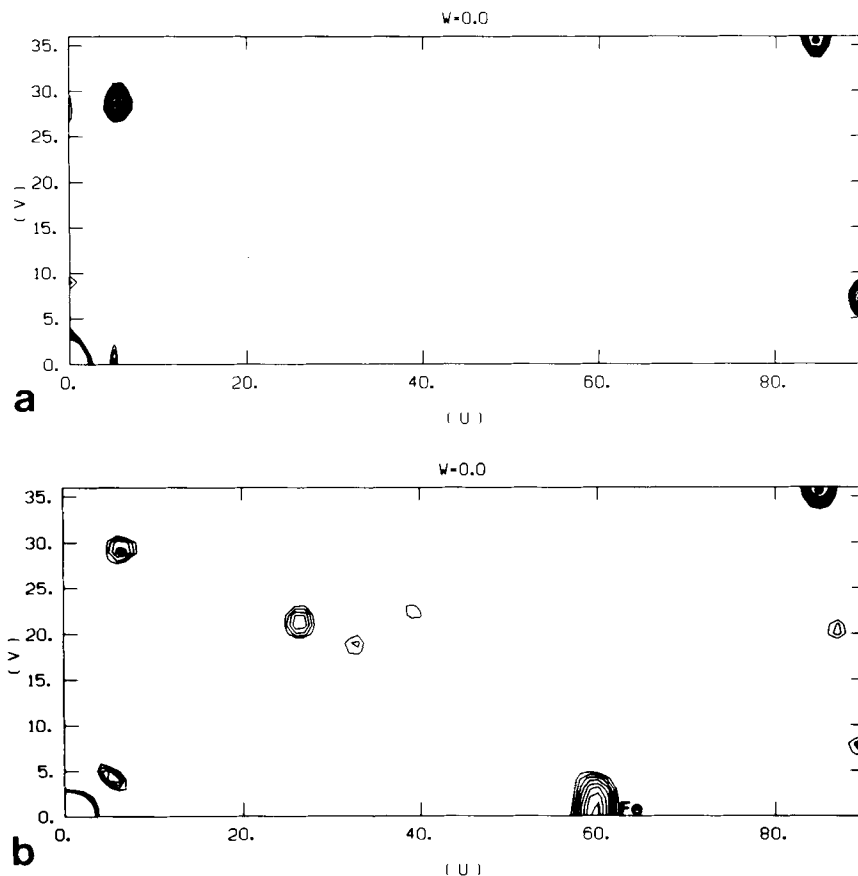


Fig. 1. Difference Patterson maps for Hg derivative of aconitase. Maps are calculated on a  $180 \times 72 \times 80$  grid; individual sections on  $W$  show one-half of a unit cell on  $U$  and  $V$ . **a**: Isomorphous difference map for all data to 3.5 Å resolution (12,125 reflections); contoured with 10 levels on the highest nonorigin peak; first contour omitted;  $W=0.0$  section showing three self-

vectors for the Hg1 site (o);  $U=1/2$  and  $V=1/2$  vectors occur in this section because  $z=0.51$ . **b**: Anomalous difference map for all data to 5.0 Å resolution (3,313 acentric reflections); contoured with 9 levels on the highest nonorigin peak; first contour omitted;  $W=0.0$  section showing three self-vectors for Hg1 site (o) and self-vector for Fe-S cluster (Fe).

$\leq 3.0$  Å, in agreement with the EXAFS data.<sup>14</sup> The Fe-S cluster as modeled from the 2.7 Å anomalous difference Patterson map<sup>33</sup> was refined as a single site against the 4.0 Å data using the origin-removed Patterson map method.<sup>40</sup> Using this one-site model, phases were calculated and refined using the iterative single anomalous scatterer (ISAS) method.<sup>41</sup> The correct hand of the average  $\langle \text{Fe} \rangle$  site was tested by comparing the figure of merit and map-inversion  $R$  value. With these phases it was possible to delineate the boundary of the molecule and packing scheme at 5.0 Å resolution.

The film apo derivative isomorphous data (Table I) was then evaluated with difference Patterson maps to 3.0 Å resolution. At 5.0 Å resolution the map revealed three vectors at the same coordinates as observed for the native anomalous difference Patterson map,<sup>33</sup> but with even greater contrast. At 3.0 Å the vector distribution on and near the Harker sections closely followed that of the 2.7 Å anomalous difference map. Consequently, the apoprotein isomorphous derivative complemented the native

anomalous data. A single  $\langle \text{Fe} \rangle$  site was refined against the isomorphous differences at 3.5 Å (Table I) and used for iterative single isomorphous replacement (ISIR) phase calculations<sup>41</sup> in combination with the ISAS phases. The resulting electron-density map revealed short segments of  $\beta$ -strands and right-handed  $\alpha$ -helices but was not interpretable. However, refinement of the Fe-S cluster as a single  $\langle \text{Fe} \rangle$  site against the multiwire area detector anomalous and apoprotein isomorphous data confirmed the results of the film data analysis.

ISAS/ISIR phases based on the  $\langle \text{Fe} \rangle$  site and the film data were applied to a trial set of Hg film data, revealing two sites in an isomorphous difference Fourier map. The two sites were confirmed in the isomorphous difference Patterson map using the multiwire area detector data for the Hg derivative (Fig. 1a). The correlation of the Hg sites to the  $\langle \text{Fe} \rangle$  origin was confirmed in the anomalous difference Patterson map using data from the Hg soaked crystal (Fig. 1b). The positions of seven Pt sites were similarly derived using the ISAS/ISIR phases and

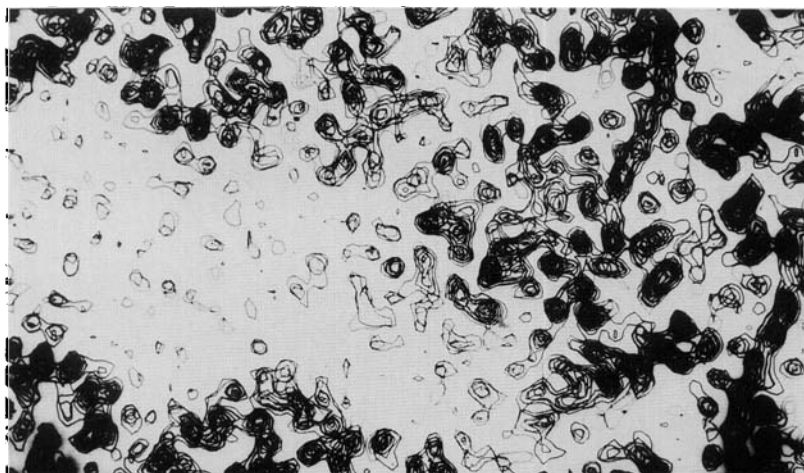


Fig. 2. Composite of five sections of the 3.0 Å MIR map contoured in seven levels with respect to the highest density. The area shown encompasses 0.7 of the unit cell along *a* (horizontal) and a full cell along *b* (vertical). Two-fold axes parallel to *c* are

located at the center right and left of the area contoured. Density for  $\alpha$ -helix and  $\beta$ -sheet segments are apparent near the 2-fold axis to the right.

confirmed in the isomorphous difference Patterson map for this derivative. Application of the phases to complete 2.7 Å film data sets for  $\text{K}_2\text{OsO}_2(\text{OH})_4$  and  $\text{Pb}(\text{NO}_3)_2$  soaked crystals failed to reveal any discrete binding sites, except for a weak binding site by  $\text{Pb}^{2+}$  adjacent to the [3Fe-4S] cluster.

The Hg and Pt sites were refined against the origin-removed isomorphous difference Patterson map.<sup>40</sup> The heavy atom parameters are summarized in Table I. For the Hg derivative data to 3.0 Å, the average ratio of  $f_H/E^*$  was 1.75 and  $R_c^†$  was 0.52; for the Pt derivative to 4.5 Å the average ratio  $f_H/E$  was 1.05 and  $R_c$  was 0.64. SIR phases from the two derivatives were combined; no additional heavy atom sites were found in difference Fourier maps. The hand of the heavy atom constellation was confirmed with Bijvoet different Fourier maps.<sup>42</sup>

Efforts to include the Fe isomorphous and anomalous data from film or area detector invariably caused the iterative filtering and Fourier inversion phasing process to diverge, apparently due to differences in Fe occupancy among the several crystals used. Consequently, phases were calculated using the area detector native data only (Bijvoet pairs were averaged), the Hg isomorphous and anomalous data to 3.0 Å, and the Pt isomorphous data to 4.5 Å. The starting figure of merit was 0.56 for 16,358 reflections to 3.0 Å resolution. Three filters were computed with the Wang procedure assuming 50% sol-

vent content; the phases were refined four cycles with the first and second filter and eight cycles with the third filter and extended to unobserved reflections.<sup>41</sup> For 18,992 reflections to 3.0 Å following phase refinement the figure of merit was 0.76.

With respect to the final model (see below), all seven of the Pt sites are located adjacent to the side chains of histidines on the surface of the protein (residues 693, 242, 14, 307, 693, 380, and 275 for Pt sites 1-7, respectively). Pt sites 1 and 5 are 2.7 Å apart and apparently represent two mutually exclusive modes of binding to  $\text{H}_{693}$ . The Hg1 and Hg2 sites are adjacent to the S $\gamma$  atoms of two cysteine residues on the surface of the protein, residues 306 and 384, respectively.

### Phase Combination

A section of the 3.0 Å MIR map is shown in Figure 2. Upon inspection of a minimap plot of the electron density it was clear that a number of  $\alpha$ -helices and  $\beta$ -strands could be interpreted. However, there were also ambiguous regions of density in turns and at connections between the segments of secondary structure. Therefore, it was necessary to build a partial model into the obvious portions of the density, and use the phase information from the partial model to improve the electron density.

The MIR map was interpreted with the program Frodo<sup>43</sup> using stereochemically restricted segments of polyalanine  $\alpha$ -helices and  $\beta$ -strands. The initial model comprised 2200 atoms. Structure factors calculated from this model were scaled in shells of  $\sin \theta/\lambda$  with an anisotropic shape factor. Figures of merits and phase probabilities for the calculated phases were derived from the agreement of  $|F_o|$  and

\* $f_H$  is the calculated heavy atom structure factor;  $E$  is the lack of closure error.

† $R_c = \sum_h (| |F_{PH}| - |F_P| | - |f_H| |) / (|F_{PH}| + |F_P|)$  where  $|F_{PH}|$  and  $|F_P|$  are the derivative and native structure amplitude, respectively, and  $|f_H|$  is the calculated heavy atom structure amplitude, for centric reflections.

$|F_c|$  by the method of Sim.<sup>44</sup> The MIR and calculated phases were then combined using weighted coefficients as suggested by Stuart and Artymuk<sup>45</sup> which minimizes bias from the model but reinforces correct features of the MIR map. For reflections at less than 7 Å resolution, only the MIR phases were used. The MIR phases were down-weighted to reflect the starting figure of merit of 0.56 prior to solvent flattening.

The procedure was iterated through four cycles of model building and editing followed by phase combination. At each cycle less than half of the working model was checked, edited, or rebuilt. During this process residues were added in turn regions as well as to  $\alpha$ -helices and  $\beta$ -strands. For about one-half of the residues, side chains were modeled where the density warranted it. The combined figure of merit gradually increased from 0.60 to 0.69 while the *R*-factor for the partial model decreased from 0.58 to 0.46. The average phase shift from the MIR and calculated phases was 29° and 31°, respectively, from the combined phase. At this stage, the model consisted of 4805 atoms; the Fe-S cluster was not included in the model. Figures 3a, b and 4a, b show portions of the 3.0 Å MIR and combined coefficients maps for  $\beta$ -sheet and  $\alpha$ -helix regions with the model of the refined structure superposed.

At this point in the analysis, the sequences of seven unique cysteinyl-tryptic peptides for beef heart aconitase became available.<sup>30</sup> Because these peptides contained cysteines as well as three methionines, a 3.0 Å Bijvoet difference Fourier map for the native crystals was calculated using the MIR phases (Fig. 5a, b). The map contained 30 significant peaks above the background; three of these were clustered within a region of clear protein density. Examination of the combine map in this region revealed that the entire sequence of peptide #9 of reference 30 (35 residues) could be accommodated to the working model without change in polarity of the chain or loss of  $\alpha$ -carbon register to the sequence. The sequence of this peptide contains two methionines and two cysteines; for each sulfur-containing amino acid a significant peak was observed for the sulfur position in the 3.0 Å Bijvoet difference Fourier map based on the MIR phases. The residues identified were C<sub>251</sub>, M<sub>254</sub>, C<sub>258</sub>, and M<sub>260</sub> (sequence numbers from the final model). While it was necessary to replace the side chains of more than half of the residues derived from the density to correct the sequence, all of these substitutions were consistent with the electron density. In addition, a pig heart aconitase peptide containing the sequence TSVFPYNHRM<sup>32</sup> could be overlapped in the density with the C-terminus of the 35 residue beef heart cysteinyl-tryptic peptide. The sulfur of the methionine in this sequence (M<sub>277</sub>) was also present in the Bijvoet difference Fourier map. Figure 5a shows the sulfur peaks of C<sub>251</sub>, M<sub>254</sub>, and M<sub>277</sub>. Figure 6a

shows the MIR electron density for the sequence ending in M<sub>277</sub>.

Subsequently, the remaining cysteinyl-tryptic peptides<sup>30</sup> were identified and aligned with the electron density in the 3.0 Å combine map by first searching the Bijvoet difference Fourier map for high peaks and then comparing the density-derived sequence to the peptide sequence. The additional seven cysteines and one methionine each had sulfur peaks in the Bijvoet difference Fourier map. Figure 6b shows the MIR electron density for the sequence PSTIHC<sub>100</sub>DHLI, which is contained within peptide #5 of reference 30.

In the process of aligning the cysteinyl-tryptic peptide sequences no errors were found in chain polarity or  $\alpha$ -carbon position of the working model. In general, Trp, Arg, Tyr, Phe, and Pro side chains as well as the Cys and Met residues were correctly or closely estimated from the experimental electron density; 196 residues were fit to the 3.0 Å combine map in this manner. Subsequently, it was found that the beef heart aconitase sequence is 98% identical with the pig heart sequence<sup>31</sup> with all differences occurring at residues exposed on the surface of the protein. None of the sequence differences involves cysteines or methionines.

### Phase Extension and Refinement

The model consisting of the 196 residues of the beef heart cysteinyl-tryptic peptides and approximately 400 residues of polyalanine or density inferred sequence was used to extend the phases to 2.85 Å. Calculated structure factors were scaled to the merged 2.1 Å native data (Table II) and these data were used throughout the refinement. For reflections in the range 3.0–2.85 Å, the calculated figure of merits and phase probabilities were determined by the method of Sim<sup>44</sup> and the Fourier coefficients were  $(2|F_o| - |F_c|)$ . Two cycles of model adjustment and phase combination were performed at 2.85 Å resolution improving the combined figure of merit to 0.75 and decreasing the *R*-factor for the model to 0.43.

The model was subjected for the first time to refinement using the program X-plor,<sup>46</sup> which reduced the *R*-factor to 0.35. In this refinement the atomic positions were refined by conjugate gradient minimization without the molecular dynamics and simulated annealing steps. An overall *B*-factor of 16.0 Å<sup>2</sup> was used. The calculated phases to 3.0 Å resolution were restrained to the MIR phases with a square-well potential with limits defined by  $\cos^{-1}(m_{\text{MIR}})$ . In addition, no weighting scheme as a function of  $\sin \theta/\lambda$  was used. The new coordinates were used to calculate phases to 2.7 Å resolution, and the model was adjusted in the combine map and again refined. Iteration of this procedure reduced the *R*-factor to 0.33 and then 0.32. The model refitting and editing steps were not exhaustive; i.e., only those

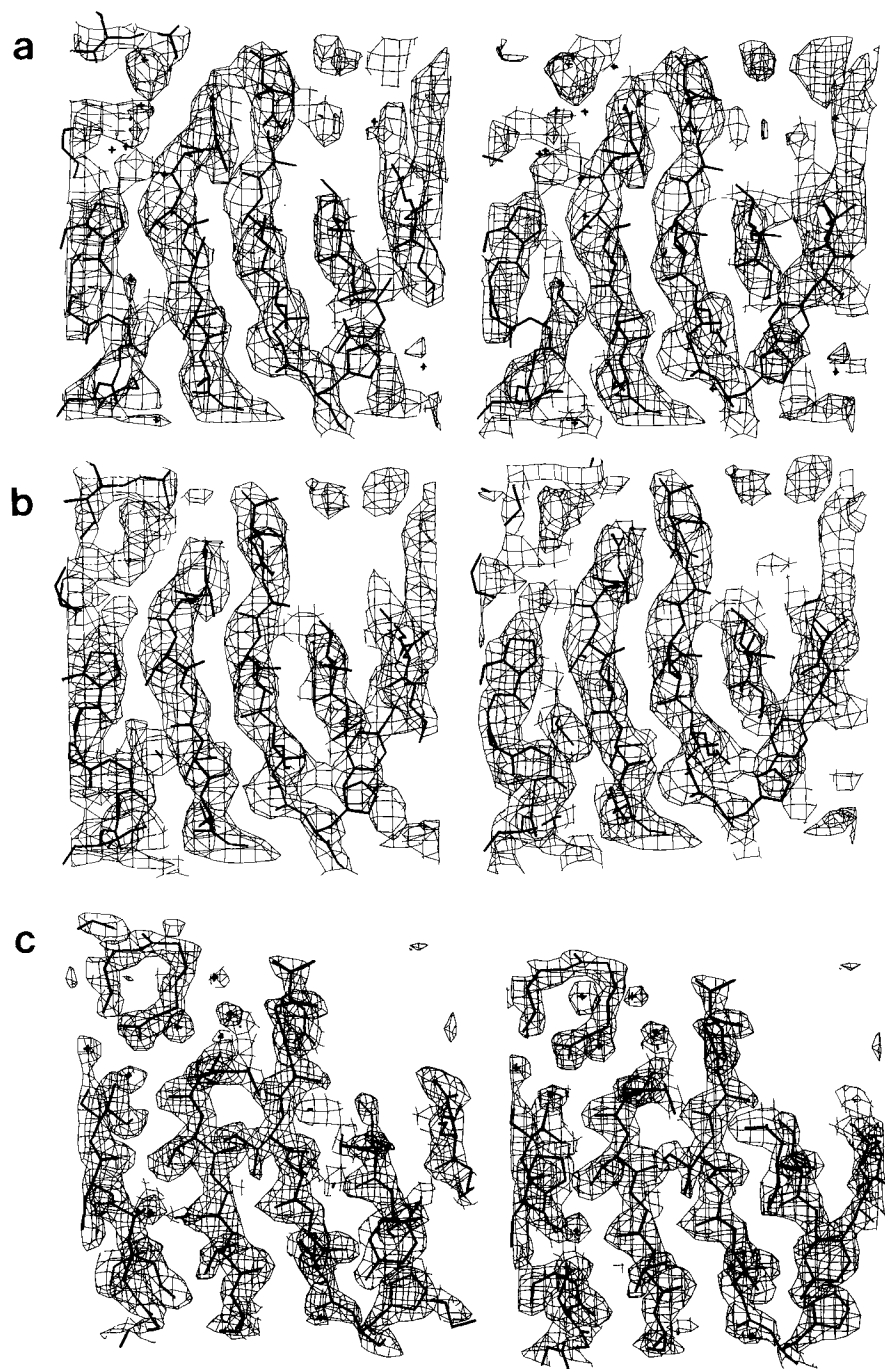


Fig. 3. A portion of the  $\beta$ -sheet within domain 2 centered on residue 238 with density from (a) the 3.0 Å MIR map, (b) the 3.0 Å combined coefficients map, and (c) the 2.1 Å  $2|F_o| - |F_c|$  map weighted with Sim figure of merits. The maps are contoured at

0.14, 0.14, and 0.22 of the maximum density in (a), (b), and (c), respectively. Note the break in the density for the strand at the left in (a), where there is continuous density in (b). Coordinates of the refined structure are superposed on the density.

residues clearly requiring adjustment, or having new density which could easily be interpreted, were rebuilt. In general, this amounted to less than a third of the entire model in a given cycle of phase extension and refinement. However, all residues were checked after each refinement cycle.

The phases were then extended to 2.6 Å. At this time the sequence of the C-terminal 461 residues became available from the DNA sequence derived from the pig heart aconitase gene.<sup>31</sup> Using the 2.6 Å map and this information it was possible to connect all five of the beef heart cysteinyl-tryptic peptides



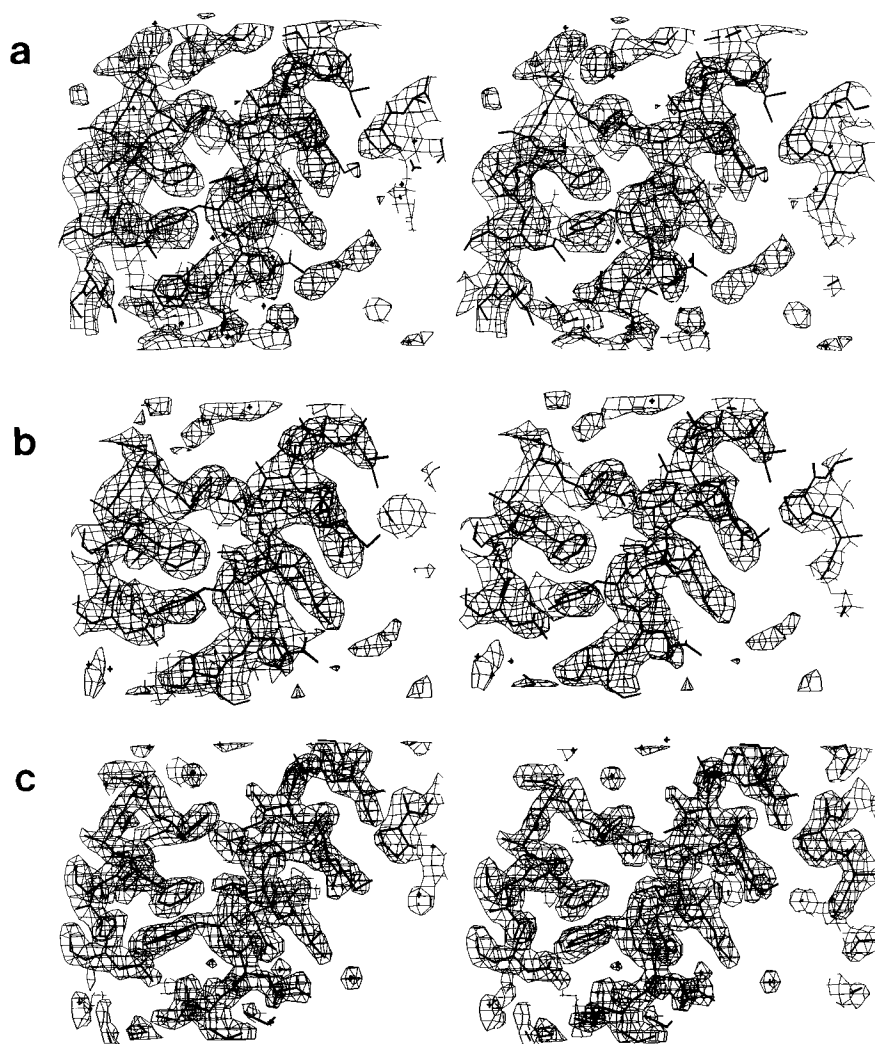


Fig. 4. Two  $\alpha$ -helices in the first domain; figure centered on residue 22. The 3.0 Å MIR (a), 3.0 Å combine coefficients (b), and 2.1 Å  $2|F_o| - |F_c|$  (c) maps are shown contoured as in Figure 3.

embedded in the C-terminal sequence (peptides # 3, 4, 7, 8, and 10 of reference 30), while fitting the correct sequence to the model for the intervening residues. No major changes in chain trace of the working model were required, but the new sequence data allowed connections to be made in loops and turns where the density alone was still ambiguous. In particular, an exposed antiparallel  $\beta$ -ribbon of residues 490–505 was interpreted. As before, all the cysteine and methionine side chains in this portion of the structure (residues 295–755) were confirmed in the 3.0 Å Bijvoet difference Fourier map. Because all three cysteine ligands to the  $[3\text{Fe}-4\text{S}]$  cluster were now in the model (cysteines 359, 422, and 425), the Fe–S cluster was fit to the density and included in structure factor calculations.

Phase extension to 2.5 Å, model adjustment, and refinement through five iterations reduced  $R$  to

0.28; the combined figure of merit was 0.78. The additional cycles were required because of the greater detail in the 2.5 Å combine map. At this point the model had the correct sequence and chain trace for residues 306–755 while the N-terminal model consisted of one peptide of 295 residues unlinked to the C-terminus at residues 296–305, a segment of the chain on the surface of the protein connecting the second and third domains. A complete 755 residue sequence from the DNA then became available.<sup>31</sup> The N-terminal model and chain trace together with the 3.0 Å Bijvoet difference Fourier map correctly predicted the locations of all six cysteines and eight methionines in residues 1–295 of the sequence. In other words, the  $\alpha$ -carbon positions of all 14 sulfur-containing amino acids in the working model for residues 1–295 proved to be in register with the true sequence. In addition, the model had

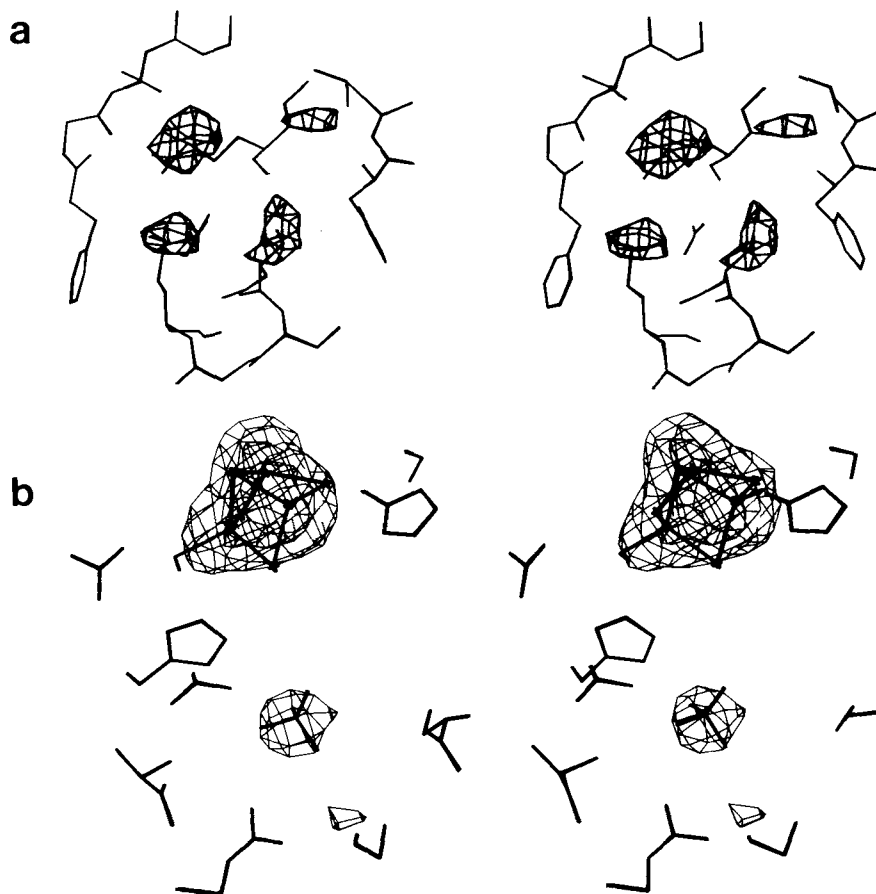


Fig. 5. Bijvoet difference Fourier map computed with 3.0 Å resolution MIR phases and native data anomalous differences. Contoured at 0.33 and 0.67 of the maximum density. **a**: Three sulfur peaks in the protein (Cys<sub>251</sub>, lower right, Met<sub>254</sub>, lower left, and Met<sub>277</sub>, upper left); and **b**: the [3Fe-4S] cluster and adjacent SO<sub>4</sub><sup>2-</sup> ion.

peptides #5 and 9 of the beef heart peptide sequences<sup>30</sup> correctly placed. Altogether, each of the 23 sulfurs of the protein, as well as the Fe-S cluster and a bound SO<sub>4</sub><sup>2-</sup> ion (Fig. 5b), was present among the highest 30 peaks in the 3.0 Å Bijvoet difference Fourier map. This map contained no bias from the model, being based on experimentally measured Bijvoet differences and MIR phases, and therefore confirmed the phase combination, extension, and refinement process.

Figure 6c shows two segments in the N-terminal sequence superposed in the starting 3.0 Å MIR density. The 2.5 Å combine map was used to correct the model for the remainder of the sequence in residues 1–295 and to link the two large peptides at residues 296–305. The completed model was used for phase extension in steps of 0.1 Å to the 2.1 Å data (Table II). At each step the model was checked and adjusted to a combine coefficients map, refined to accommodate the new data and refined again to incorporate the new features of the model. The *R*-factor was 0.28 for all observed data in the range 5.0–2.1 Å with an

overall *B*-factor of 16.0 Å<sup>2</sup>, no solvent molecules in the model, and a combine figure of merit of 0.80.

The partially refined structure was further refined with X-plor by molecular dynamics and simulated annealing.<sup>46</sup> The model was heated to 2000°K, evaluated at 1 fsec timesteps for a total of 1 psec, and annealed (cooled) in increments of 50°C (200 timesteps of 1 fsec) to 300°K. The MIR phase restraints were removed and no weighting scheme was applied. Restraints applied to the Fe-S cluster were distances, Fe-Fe 2.75 Å, Fe-S, S<sub>γ</sub> 2.31 Å; angles, S-Fe-S, S<sub>γ</sub>, 109.4°, Fe-S-Fe, 75°, Fe-S-γ-Cβ, 109.4°. The *R*-factor dropped to 0.262; refinement of individual isotropic *B*-factors reduced the *R*-factor to 0.237.

A 2.1 Å resolution map with 2  $|F_o| - |F_c|$  coefficients weighted with Sim figure of merits was used to check the entire sequence, and to identify peaks due to bound water molecules. Potential water sites were required to have at least one hydrogen bond to the protein. A large residual peak in the active site was modeled as an SO<sub>4</sub><sup>2-</sup> ion (see below, and Fig.

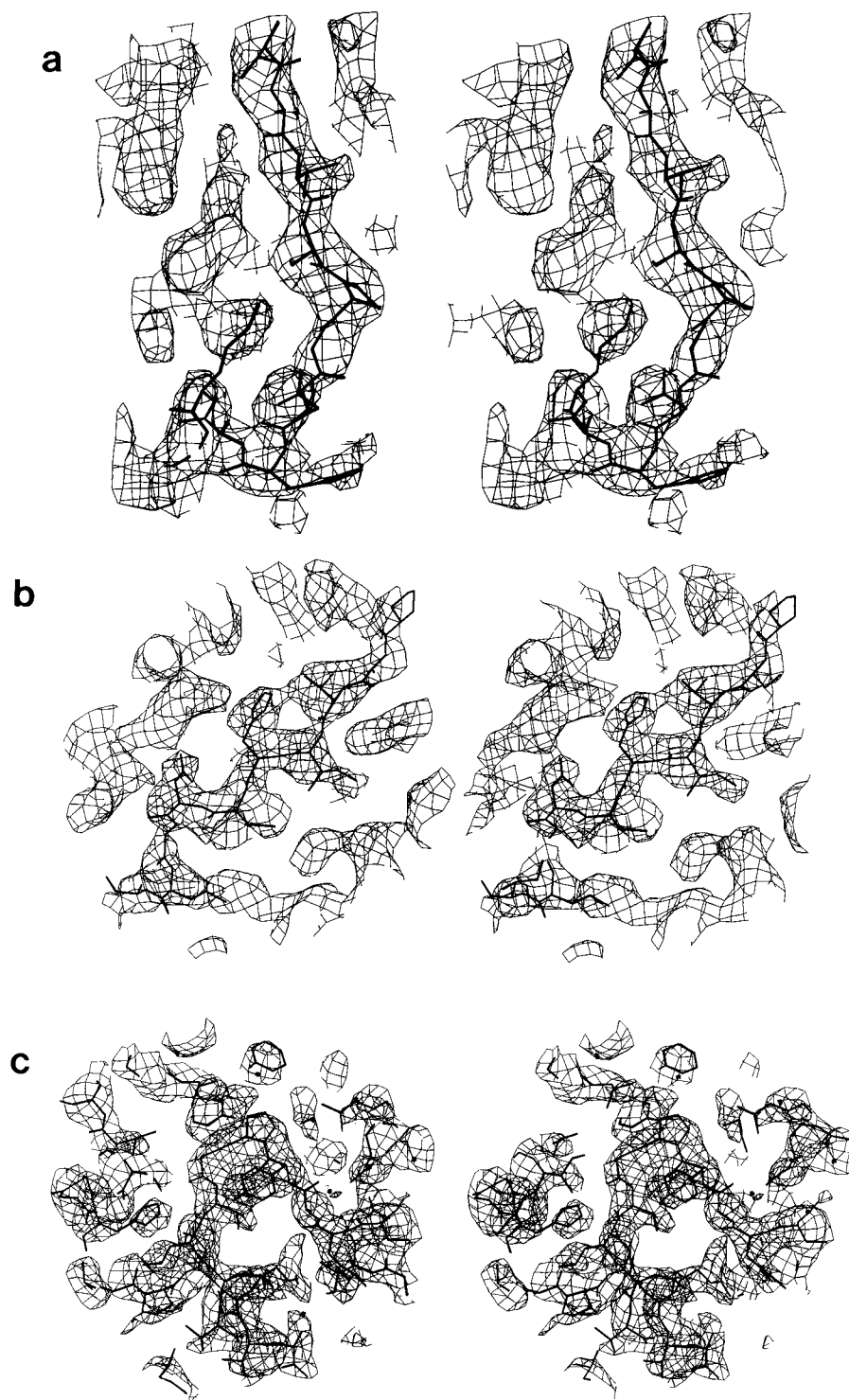


Fig. 6. The 3.0 Å MIR map contoured at 0.14 of the maximum density and showing density for three peptide sequences identified at different stages of the analysis (see text). **a:** T<sub>268</sub>SVFPYNHRM<sub>277</sub>; density for the side chains of the S, F, Y, and R in the sequence are out of the plane of the figure.

**b:** P<sub>95</sub>STIH C<sub>100</sub> DHLI<sub>104</sub>; density for H<sub>102</sub> side chain not shown. **c:** N<sub>154</sub>YAYPGVLLI<sub>163</sub> (center right to lower left); P<sub>67</sub>DRVA<sub>71</sub> (center left to lower center), and isolated peaks for H<sub>47</sub>, Y<sub>19</sub>, and Y<sub>273</sub>; density for Y<sub>155</sub> side chain not shown.

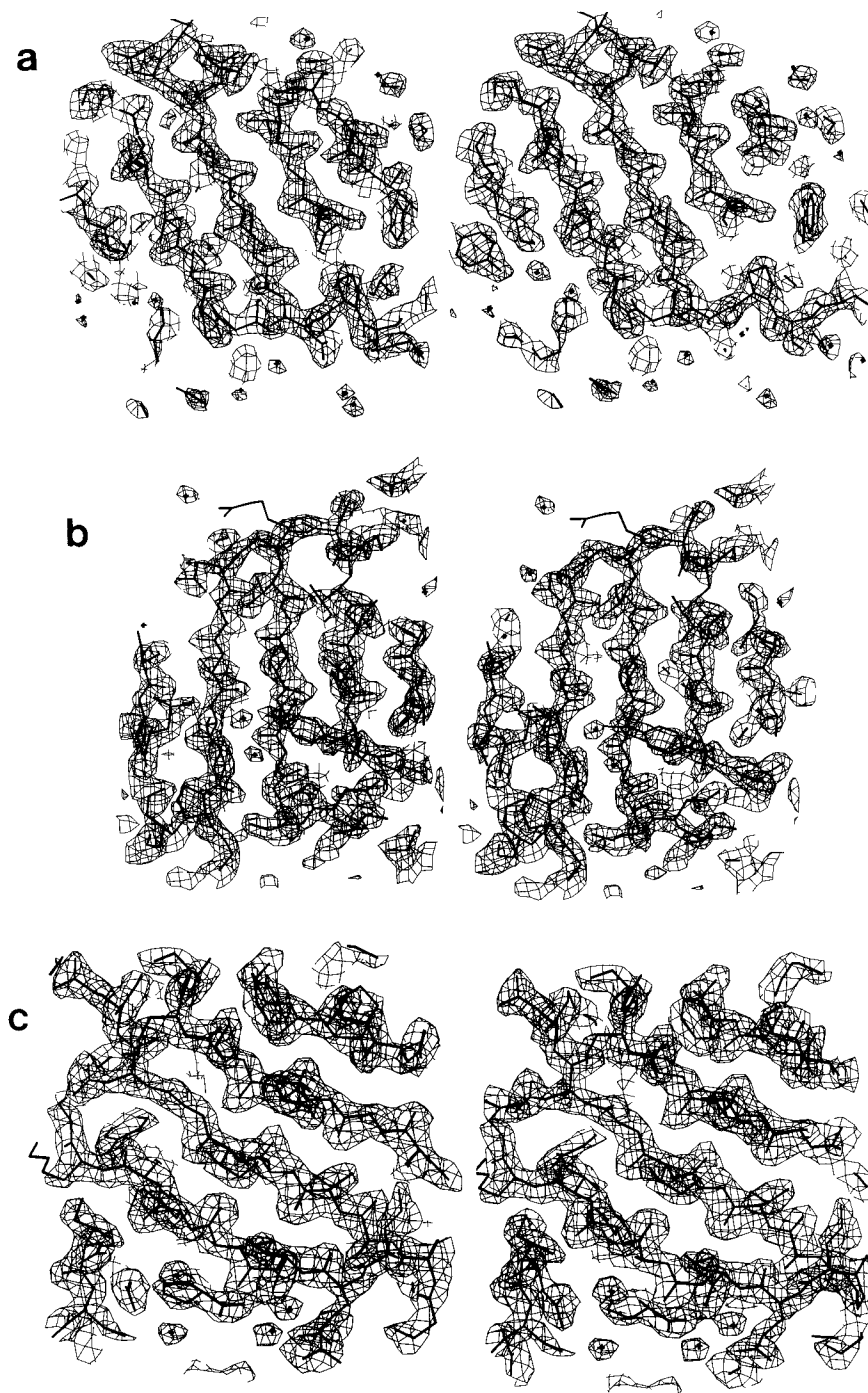


Fig. 7a-c.

5b). The refined structure has an *R*-factor of 0.209 for all observed reflections in the range 5.0–2.1 Å (Table II). The rms deviations from ideality of bonds and angles are 0.026 Å and 4.33°, respectively. The model contains 5837 protein atoms, the [3Fe–4S] cluster and  $\text{SO}_4^{2-}$ , 261 water molecules with  $B < 40.0 \text{ Å}^2$  and 61 waters with  $40.0 \text{ Å}^2 < B < 60.0 \text{ Å}^2$ . The coordinates have been deposited with the Pro-

tein Data Bank. Figure 7a–e shows portions of the final 2.1 Å map for elements of secondary structure within domains of the protein not shown in Figures 3c or 4c. Figure 8 shows the [3Fe–4S] cluster and the ligand peptide  $\text{C}_{422}\text{GPC}_{425}$  in the 2.1 Å map. Figure 9 depicts the density for the nine tryptophanes at three stages of the analysis.

It should be noted that the N-terminus of the pro-

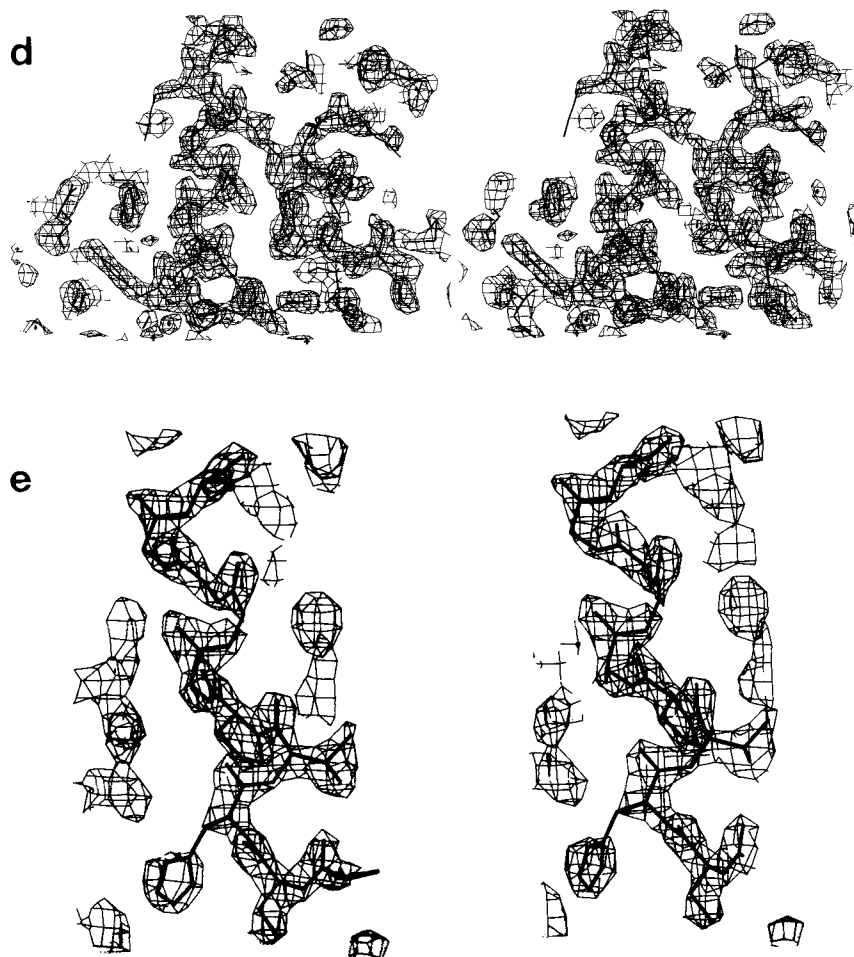


Fig. 7. Portions of secondary structure in domains not shown in Figure 3 or 4. The  $2.1 \text{ \AA } 2|F_o| - |F_c|$  map weighted with Sim figure of merits is shown contoured at 0.22 of the maximum density in (a–d) and 0.25 of the maximum density in (e). a: Domain 1  $\beta$ -sheet centered on residue 70; b: domain 3  $\beta$ -sheet centered on

residue 355; c: domain 4  $\beta$ -sheet centered on residue 634; d: domain 3  $\alpha$ -helix centered on residue 370; e: domain 1  $3_{10}$  helix with the sequence  $D_{166}SHTPNGGGL_{175}$ . Gaps in the density for  $H_{168}$  and  $G_{172}$  are connected at a contour level of 0.18 of the maximum density.

tein has not been identified from the DNA or protein sequence, or in the electron density. Residue 1 in the structure reported here is the first residue for which there is identifiable density. There are at least 24 more residues in the as yet incomplete DNA sequence<sup>31</sup>; some of these may be part of a leader sequence. The N-terminus of the mature enzyme is blocked.<sup>32</sup> While the additional residues must be disordered in the crystal, they could be accommodated in the packing scheme because a large solvent channel runs through the crystal parallel to the  $a$  axis adjacent to the present N-terminus.

### DOMAIN STRUCTURE

The structure of aconitase consists of four domains. The first three are tightly associated about the Fe–S cluster; the fourth is more loosely associated with the first three (Fig. 10). In the primary sequence<sup>31</sup> the domains consist of the following residues: 1–202, 203–320, 321–513, and 538–755. Res-

idues 514–537 comprise a linker peptide wrapping around the surface of the molecule and connecting domains 3 and 4. Figure 10a shows the extensive interface created by the association of the C-terminal fourth domain with the first three. Although this boundary appears to extend toward the solvent equally far from the point where the fourth domain nestles over the Fe–S cluster, side chains are more tightly packed at the domain interface on the side of the linker peptide, so that the principal access to the solvent from the cluster is the cleft to the right in Figure 10a. The structure suggests the possibility of hinge motion at the linker peptide which would separate the fourth domain from the first three.

Perspective views of the domains are shown in Figure 11; schematics of their folding motifs are given in Figure 12. The packing of the three N-terminal domains in relation to the central Fe–S cluster is depicted in Figures 10b and 11a. Viewed to-

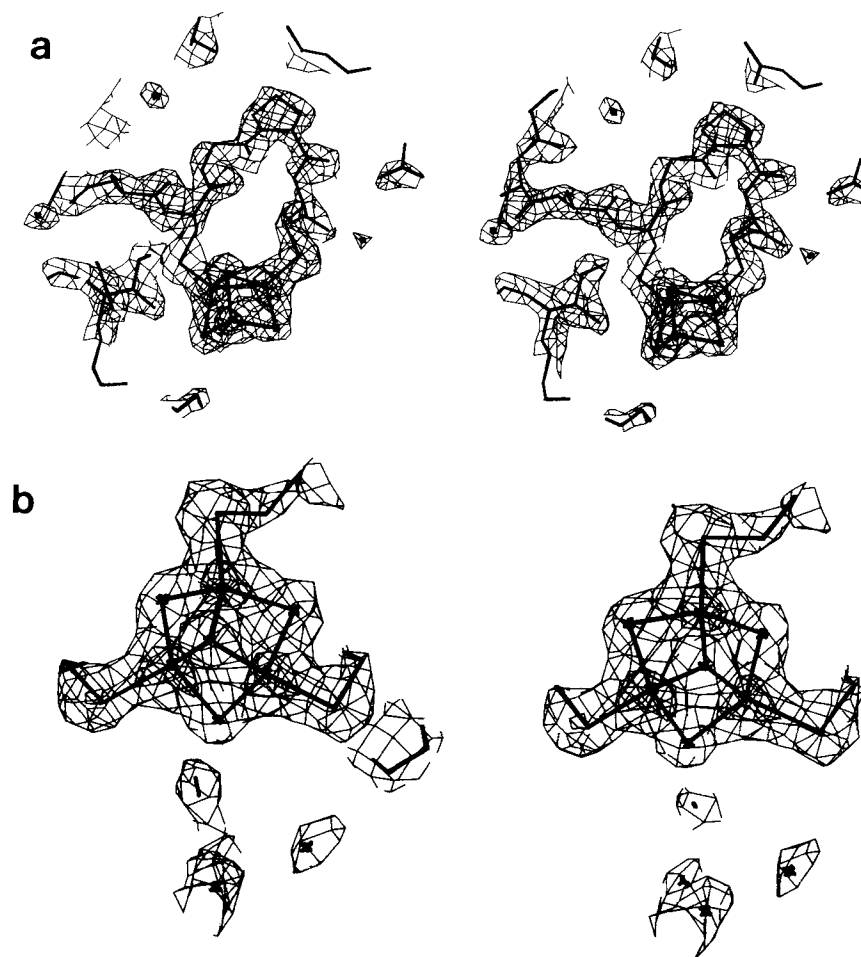


Fig. 8. The 2.1 Å  $2|F_o|-|F_c|$  map weighted with Sim figure of merits for (a) the [3Fe-4S] cluster and residues 419-425 including liganding cysteine peptide  $C_{422}GPC_{425}$ ;  $I_{146}$  at lower left; and

(b) [3Fe-4S] cluster with attaching cysteine sulfurs of  $C_{359}$ ,  $C_{422}$ , and  $C_{425}$ . Contoured at 0.25 and 0.70 of the maximum density in the map which is on Fe of the [3Fe-4S] cluster.

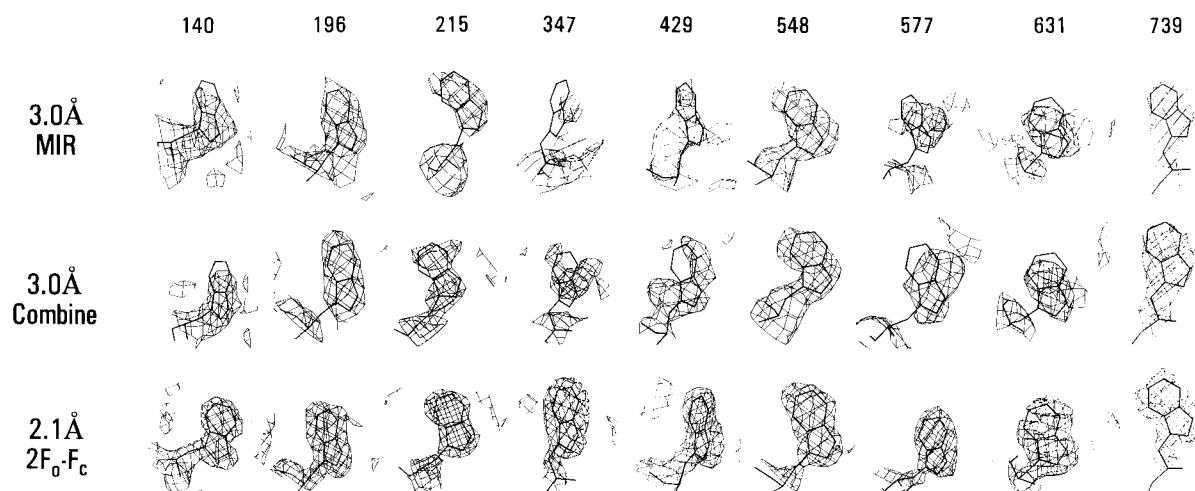


Fig. 9. The nine tryptophanes in the structure (sequence numbers across top of figure) superposed on the 3.0 Å MIR, 3.0 Å combined coefficients, and 2.1 Å  $2|F_o|-|F_c|$  maps; contoured as in Figure 3.

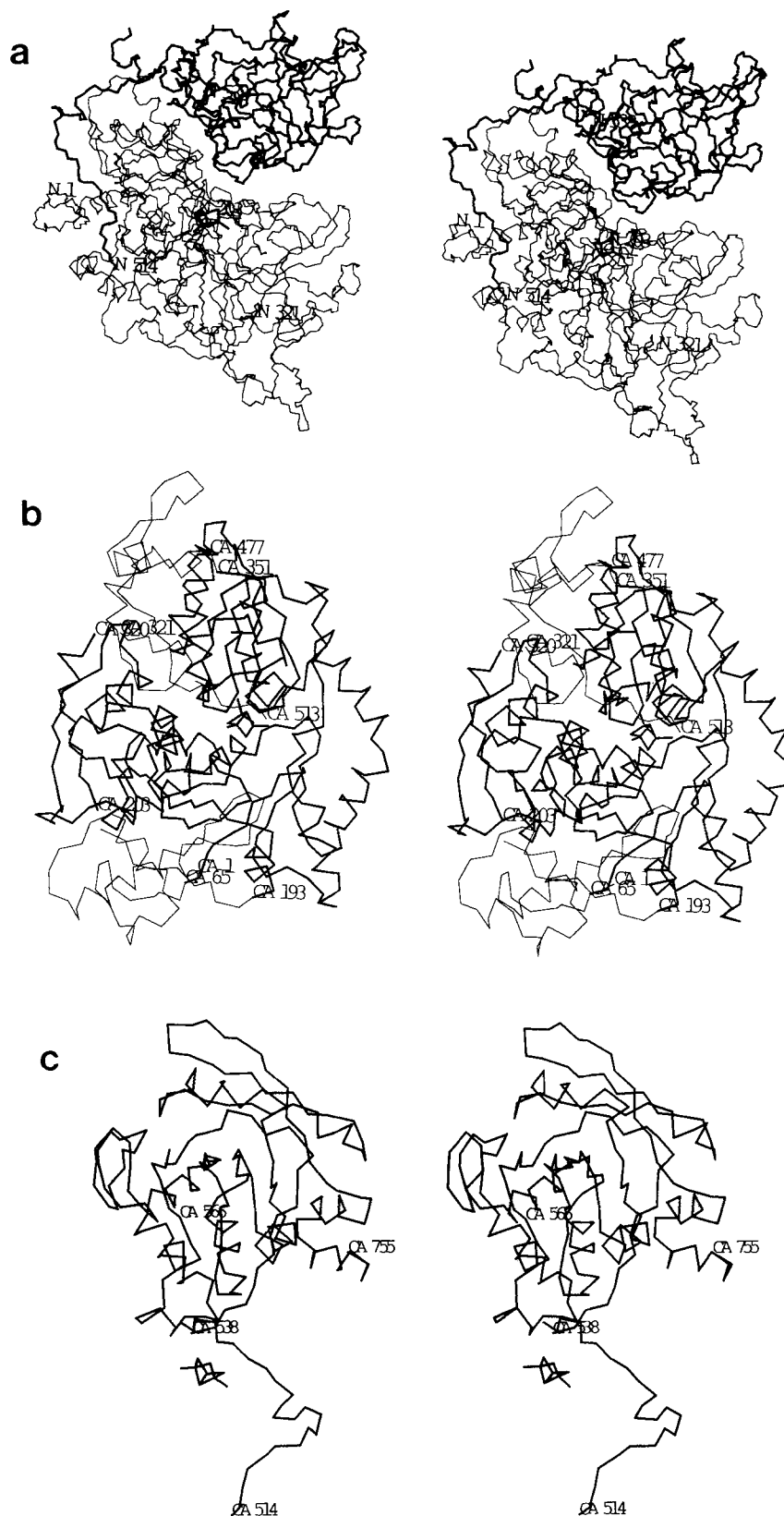


Fig. 10. Stereo diagrams of the aconitase structure. **a:** N, C $\alpha$ , and C atoms of the entire structure; the C-terminal fourth domain, linker peptide, and Fe-S cluster are shown in heavy lines. **b:** C $\alpha$  atoms of the N-terminal three domains in a view roughly orthogonal to that in (a) (each domain shown as a separate chain seg-

ment); residues of the central  $\alpha/\beta$  folding motif in each domain are shown in heavy lines. **c:** C $\alpha$  atoms of the C-terminal fourth domain, the linker sequence, and the Fe-S cluster; residue 566 is the reactive cysteine.

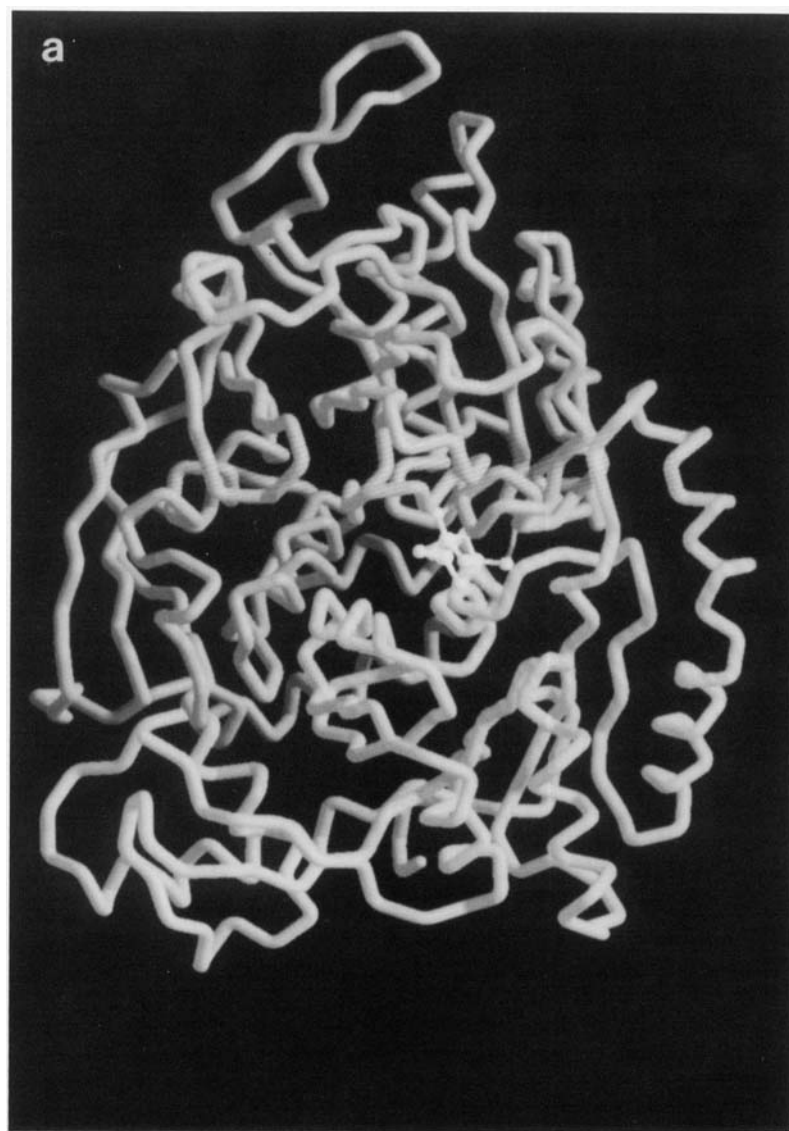


Fig. 11. Perspective views of the aconitase domains based on coordinates for the N, C $\alpha$ , and C main chain atoms and showing individual atoms for the Fe-S cluster and active site residues. **a**: The N-terminal domains and Fe-S cluster; domain 1, domain 2, domain 3, clock wise from lower right. **b**: Domain 1 with side chains of Q<sub>73</sub>, D<sub>101</sub>, H<sub>102</sub>, H<sub>148</sub>, D<sub>166</sub>, S<sub>167</sub>, and H<sub>168</sub>. **c**: Domain 2 with sidechain of E<sub>263</sub>. **d**: Domain 3 with side chains of C<sub>359</sub>,

C<sub>422</sub>, and C<sub>425</sub> to the [3Fe-4S] cluster, N<sub>447</sub> and R<sub>453</sub>, and the side chain of residue 448 (depicted as Lys, in the final model 448 is Arg). **e**: Domain 4 and the linker peptide with side chains of R<sub>581</sub>, S<sub>643</sub>, and R<sub>645</sub>. These figures prepared by M. Pique with the program MCS written by M. Connolly. Figure 11 continues on following two pages.

ward the cluster the domains pack in order N→C in a clockwise manner. The topology of the secondary structure elements of domains 1–3 contains a motif similar to that of the nucleotide binding domains of dehydrogenases (Figs. 11b–d, 12a–c); each domain contains a central parallel  $\beta$ -sheet linked by helices: +1x, +1x, -3x, (-1x, -1x).<sup>47</sup> However, the parallel  $\beta$ -sheets are composed of five, four, and five strands in domains 1–3, respectively, rather than six as often observed in dehydrogenases.<sup>47,48</sup> Superposition of the C $\alpha$  atoms of residues 1–150 of malate dehydrogenase<sup>49</sup> on aconitase domains 1, 2, and 3

shows that while the stereochemically restricted  $\beta$ -sheets superpose well, and the crossover connections between strands have the same chirality, the structures are not overall homologous in three dimensions.

Although domains 1–3 have the same secondary structure motif, additions to the structure of each domain appear to play an important role in the 3-fold association (Figs. 10b, 11a). Residues 1–64 in domain 1 preceding the parallel  $\beta$ -sheet provide contacts to domain 2, and an extra helix between two strands of the sheet (Fig. 12a) makes contacts to



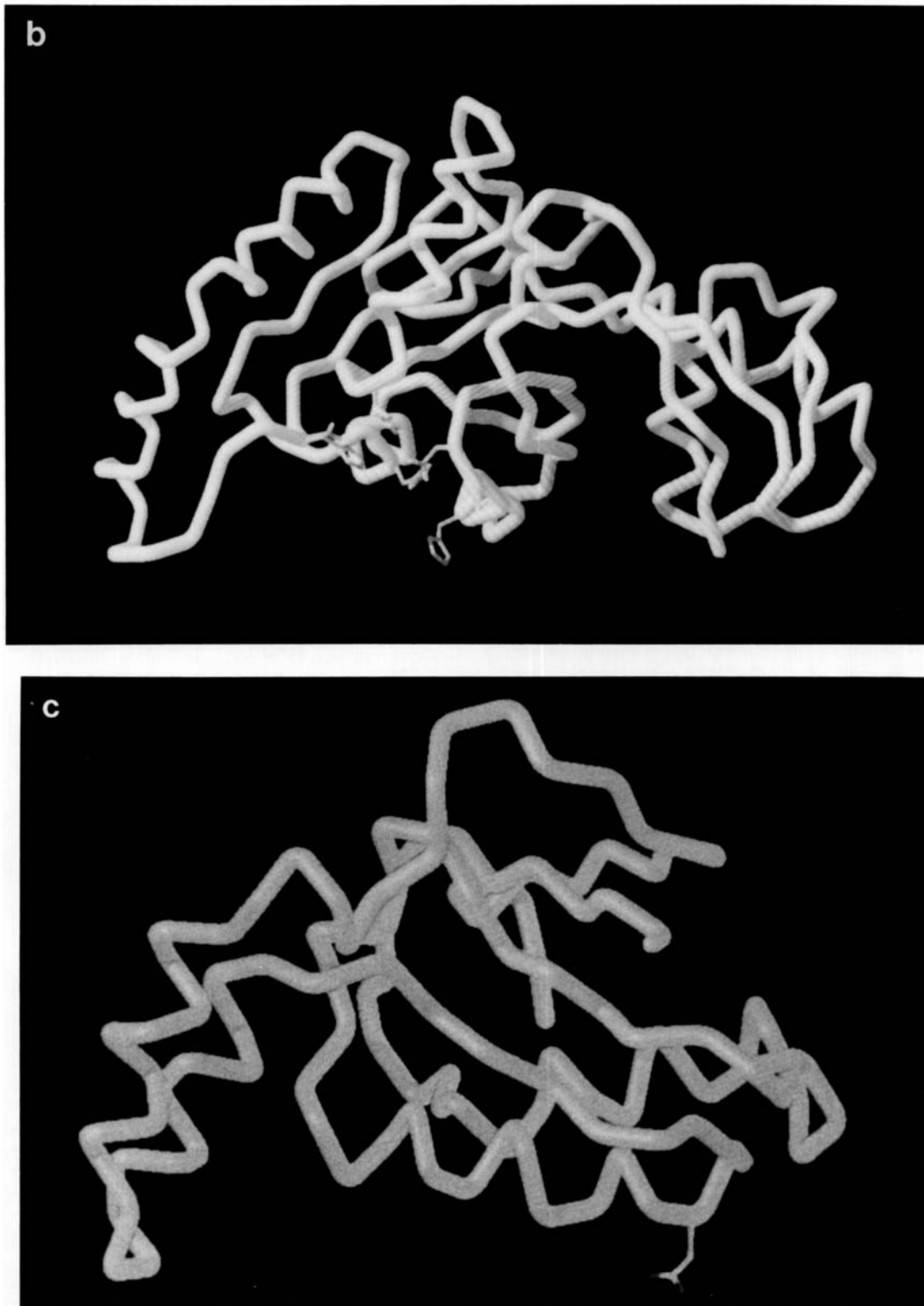


Fig. 11b-c.

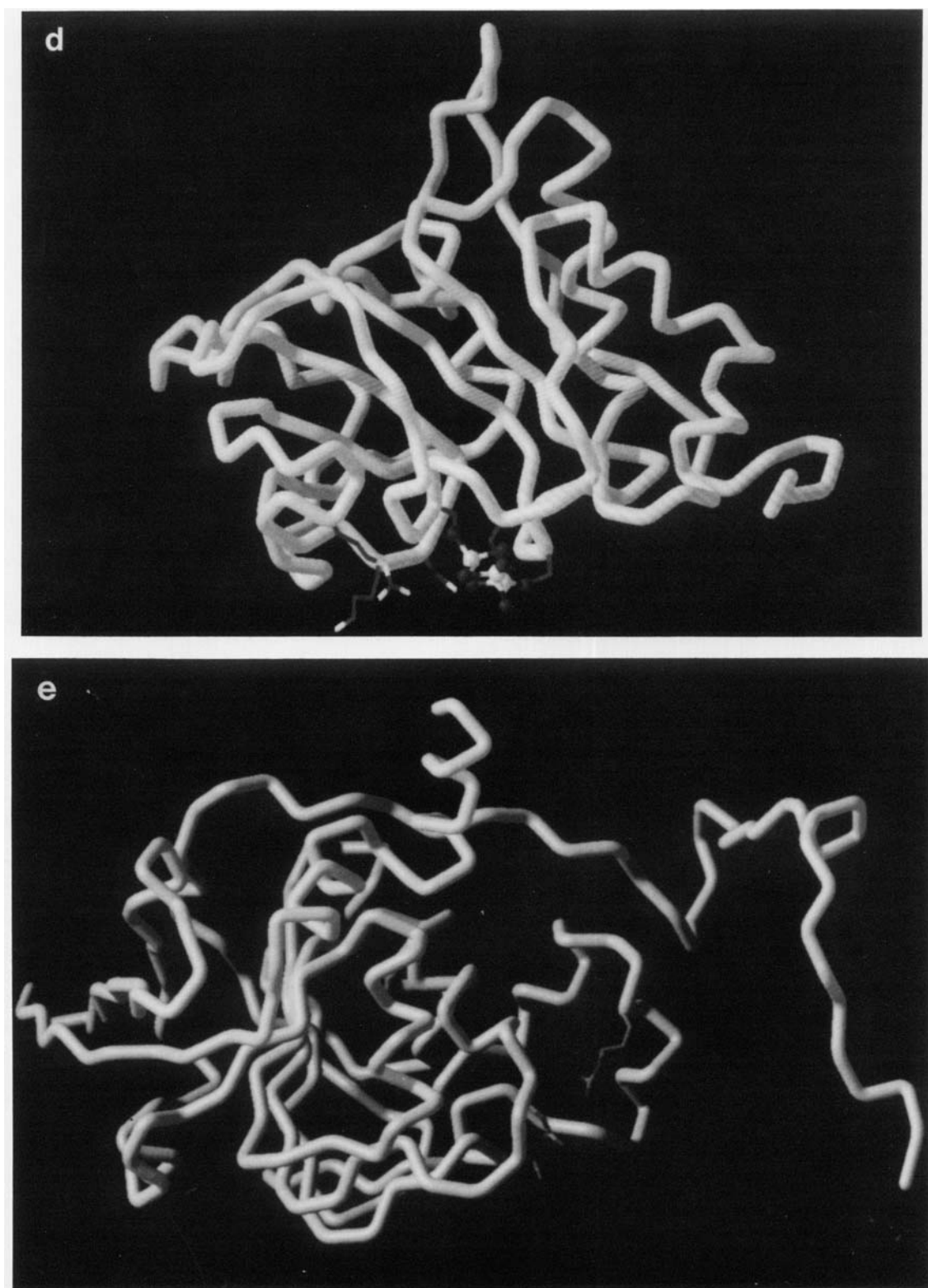


Fig. 11d-e.

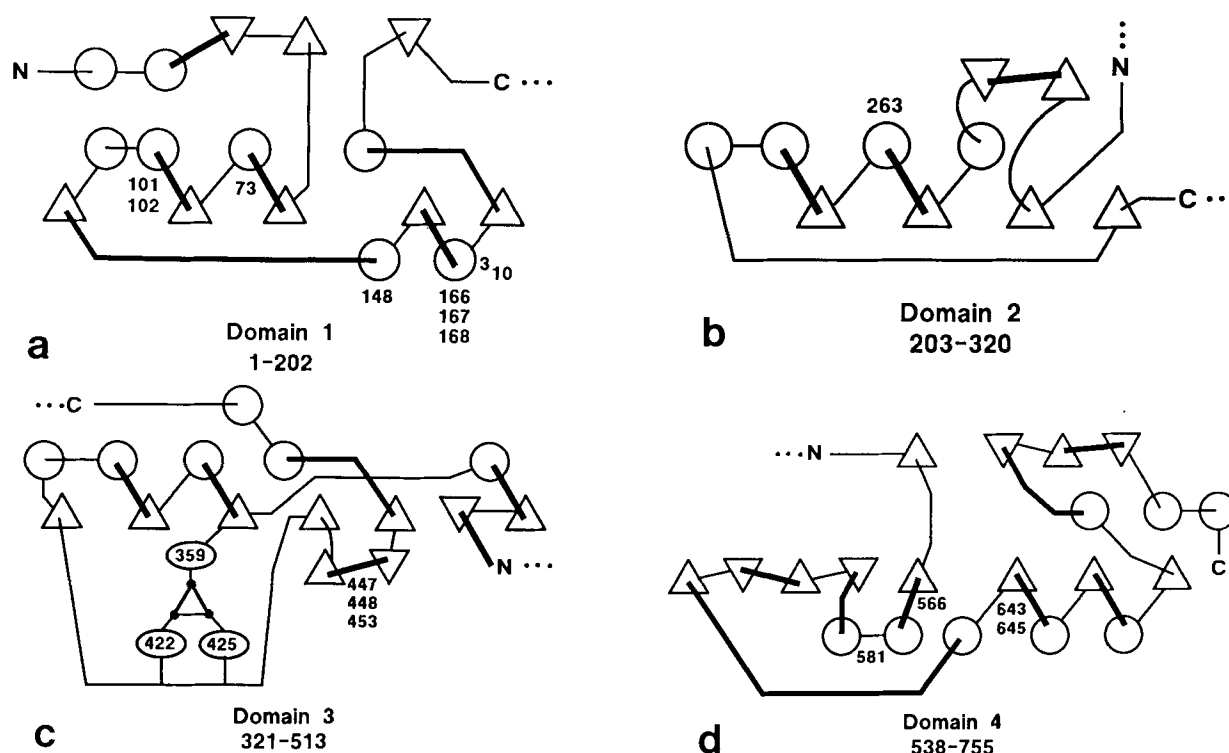


Fig. 12. **a-d**: Schematic diagrams showing the topology and secondary structure elements of the aconitase domains. Helices are represented by circles and  $\beta$ -strands by triangles. Residue

numbers in the sequence for each domain and putative active site residues are given. The  $3_{10}$  helix (**a**),  $[3\text{Fe}-4\text{S}](\text{S}\gamma)_3$  cluster (**c**), and reactive cysteine 566 (**d**) are also indicated.

domain 3. In domain 2 an antiparallel  $\beta$ -ribbon inserted between strands of the  $\beta$ -sheet in the folding motif (Fig. 12b) is in contact with domain 3. The orientation of a pair of helices at one end of the sheet allows this domain to wedge between domains 1 and 3. Residues preceding the N-terminus of the domain 3 parallel  $\beta$ -sheet are in contact with domain 2. The fourth and largest C-terminal domain (Figs. 10c, 11e, 12d) is different from the preceding three. It consists of a parallel  $\beta$ -sheet, extended at one edge by a  $\beta$ -meander, which is flanked by  $\alpha$ -helices on one side and an antiparallel  $\beta$ -sheet on the other. In this general aspect, domain 4 is like the second domain of glutathione reductase.<sup>47,50</sup>

### ACTIVE SITE ELEMENTS

The active site of aconitase contains an Fe-S cluster<sup>13-15</sup> which occurs as a  $[3\text{Fe}-4\text{S}]$  cluster in the structure reported here. Based on spectroscopic evidence, the active site must contain the Fe-S cluster. However, in the structure a  $\text{SO}_4^{2-}$  ion is bound near the  $[\text{Fe}-\text{S}]$  cluster (see below) and there is no density for a bound inhibitor (tricarbyllate). In the following discussion, it is assumed that the cavity adjacent to the  $[3\text{Fe}-4\text{S}]$  cluster containing a bound anion is the active site. In addition to the metal center, the putative active site contains structural

elements from all four protein domains. A three-turn  $3_{10}$ -helix in domain 1 packs between the preceding  $\beta$ -strand and  $\alpha$ -helix and an  $\alpha$ -helix from domain 2 (Figs. 12a, 13a, b). The  $\alpha$ -helix is inclined  $33^\circ$  to the  $3_{10}$ -helix; the two helices are antiparallel. The sequence of residues in the  $3_{10}$ -helix is  $\text{D}_{166}\text{SHTPNGGG}_{174}$ ; the side chains of  $\text{D}_{166}$ ,  $\text{S}_{167}$ , and  $\text{H}_{168}$  are oriented into the active site where the base of the helix is adjacent to the  $[3\text{Fe}-4\text{S}]$  cluster. The glycines at the end of the helix facilitate a third full turn, since the  $\phi, \psi$  angles of a  $3_{10}$  helix cause  $\text{C}_\beta$  atoms to be eclipsed.<sup>51</sup> The sequence following the helix is  $\text{L}_{175}\text{GGICIGVGG}$ .<sup>31</sup>  $\text{N}_{171}$  in the center of the  $3_{10}$ -helix participates with  $\text{N}_{259}$  and  $\text{N}_{447}$  in a chain of hydrogen bonded asparagine side chains (Fig. 13b).  $\text{N}_{259}$  is situated on the neighboring  $\alpha$ -helix;  $\text{N}_{447}$  is part of a loop carrying other active site residues. Together the asparagines flank the Fe-S cluster and may serve to tie together these elements of the structure, one from each of the three N-terminal domains.

A second element of the active site is a pair of loops in domain 3 (Fig. 13c). One is the cysteine containing peptide  $\text{C}_{422}\text{GPC}_{425}$  which provides two of the ligands to the Fe-S cluster (Fig. 12c). The other is an irregular loop which could be described as two consecutive reverse turns. The loop occurs in

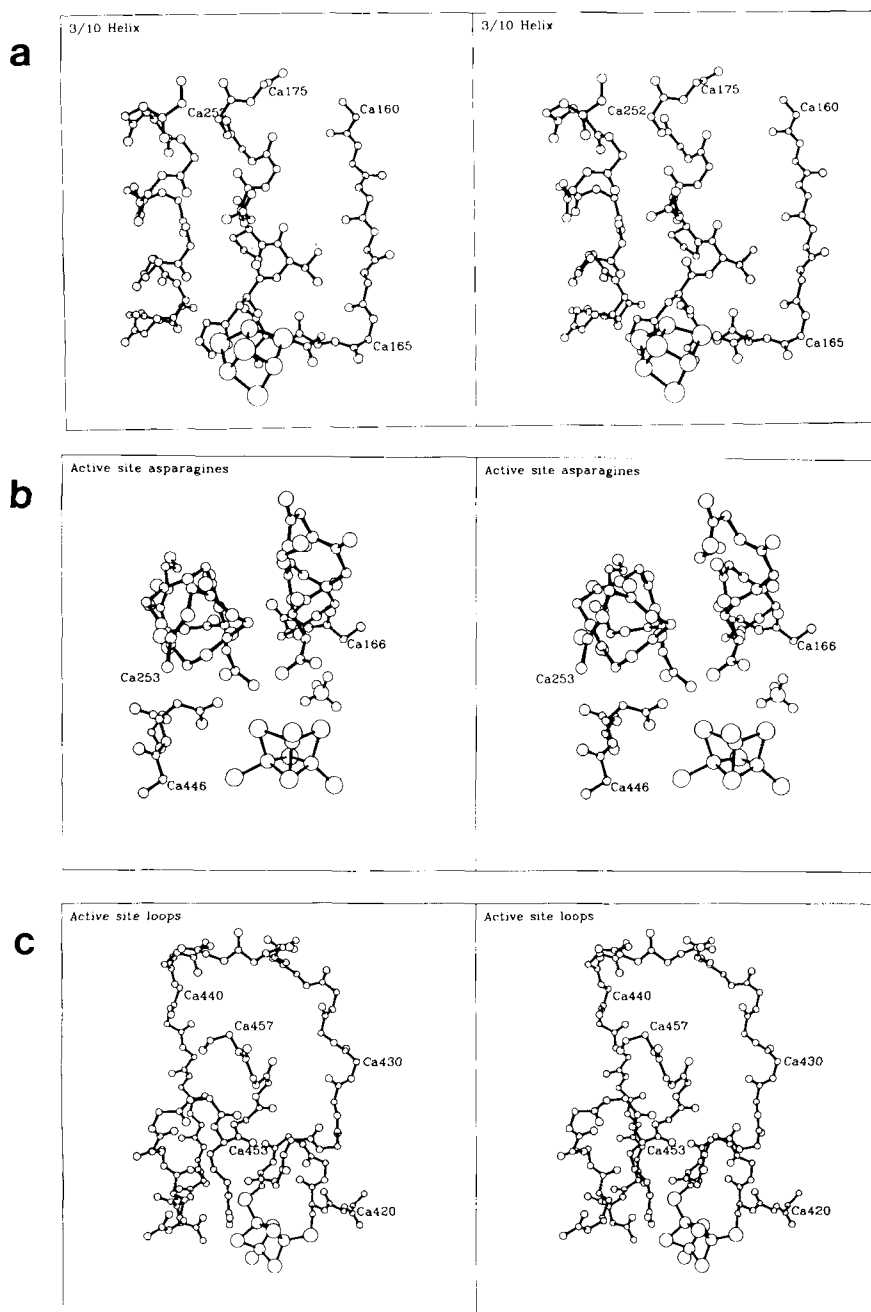


Fig. 13a-c.

the folding motif where typically an  $\alpha$ -helix would be expected (residues 446–456) (Fig. 12c). Residues from this loop within the active site are N<sub>447</sub> and R<sub>453</sub>; R<sub>448</sub> is displaced to one side.

Assuming the active site is that portion of the cleft in proximity to the Fe–S cluster and the bound anion, then the following residues may be important for catalysis: from domain 1, Q<sub>73</sub>, D<sub>101</sub>, H<sub>102</sub>, H<sub>148</sub>, D<sub>166</sub>, S<sub>167</sub>, H<sub>168</sub>, N<sub>171</sub>; from domain 2, N<sub>259</sub>, E<sub>263</sub>; from domain 3, N<sub>447</sub>, R<sub>448</sub>, R<sub>453</sub>; and from domain 4,

R<sub>581</sub>, S<sub>643</sub>, S<sub>644</sub>, R<sub>645</sub>. These side chains are shown in Figure 13d and depicted in Figure 11b–e. Each histidine is in association with an aspartate or glutamate: H<sub>168</sub> with E<sub>263</sub>, H<sub>102</sub> with D<sub>101</sub>, and H<sub>148</sub> with D<sub>166</sub>. Paired aspartate–histidine side chains have been observed in the active site of malate dehydrogenase<sup>49</sup> and three histidines are involved in binding citrate to citrate synthase.<sup>52</sup> Because of the loose association of the fourth domain with the rest of the molecule, it is possible that the enzyme in

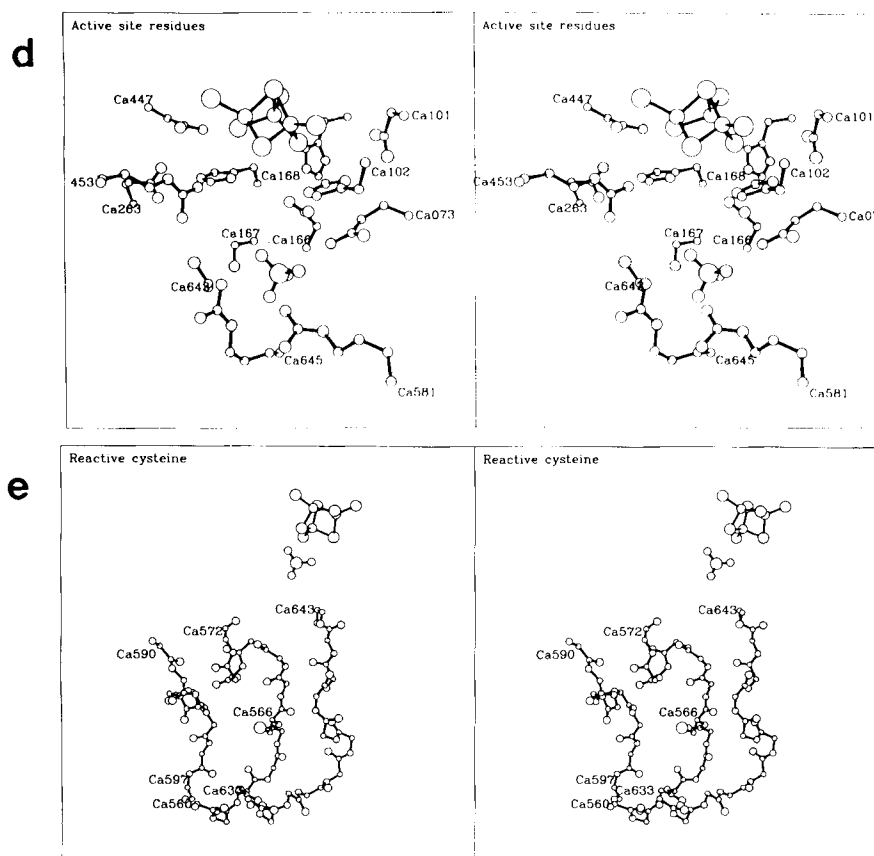


Fig. 13. Stereo figures showing elements of the aconitase structure with respect to the  $[3\text{Fe}-4\text{S}](\text{S}\gamma)_3$  cluster and bound  $\text{SO}_4^{2-}$  ion. **a:** Main chain atoms of residues 160–175 and 252–265 with side chains shown for residues 166–174 in the  $3_{10}$ -helix, D<sub>166</sub>SHTPNGGG<sub>174</sub>. **b:** Main chain atoms of residues 166–174, 253–261, and 446–448, and side chains of N<sub>171</sub>, N<sub>259</sub>, and N<sub>447</sub>. **c:** Main chain atoms of residues 420–457 and side chains for

C<sub>422</sub>, C<sub>425</sub>, N<sub>447</sub>, R<sub>448</sub>, and R<sub>453</sub>. **d:** C<sub>6</sub> and side chain atoms of Q<sub>73</sub>, D<sub>101</sub>, H<sub>102</sub>, H<sub>148</sub> (unlabeled), D<sub>166</sub>, S<sub>167</sub>, H<sub>168</sub>, E<sub>263</sub>, N<sub>447</sub>, R<sub>453</sub>, R<sub>581</sub>, S<sub>643</sub>, and R<sub>645</sub>. Not shown are side chains of N<sub>171</sub> and N<sub>259</sub> as in (b), R<sub>448</sub> as in (c), and S<sub>644</sub> which also hydrogen bonds to  $\text{SO}_4^{2-}$ . **e:** Main chain atoms of residues 560–572, 590–597, and 633–643 within domain 4 and the side chain of reactive cysteine C<sub>566</sub>.

solution adopts conformations other than the one observed in the crystal.

### IRON-SULFUR CLUSTER

The  $[3\text{Fe}-4\text{S}]$  cluster is liganded by cysteines 359, 422, and 425 in domain 3 (Figs. 8a, b, 11a, d, 12c, and 13c). The structure of the cluster is like that of a  $[4\text{Fe}-4\text{S}]$  cubane, except that one Fe is missing in the inactive form of the enzyme. The site for the missing Fe is close to hydrophilic residues, where the three divalent inorganic sulfurs of the cluster face toward the cleft and the bound  $\text{SO}_4^{2-}$  (Fig. 13d). This is consistent with the Mössbauer evidence that the fourth Fe added to rebuild the  $[4\text{Fe}-4\text{S}]$  cluster is also the Fe site which complexes to substrates.<sup>21–24</sup> Surprisingly, there is no free cysteine among the residues lining the active site, suggesting that the ligands to the fourth site Fe do not include cysteine. This is not inconsistent with the results of reactions of both inactive and activated aconitase

with sulfhydryl reagents.<sup>30,53</sup> The nearest free thiol to the cluster is C<sub>100</sub>; the S $\gamma$  atom of this cysteine is 14.3 Å from the center of the cluster. It is unlikely that C<sub>100</sub> could be a ligand, because residues 95 to 100 comprise a strand in the parallel  $\beta$ -sheet in domain 1 and are not in a flexible loop region. More plausibly, C<sub>100</sub> could be a ligand to the linear type  $[3\text{Fe}-4\text{S}]$  cluster in the high pH form of the enzyme; at this pH the cluster is transformed and the protein is known to adopt a new conformation.<sup>36</sup> Recently, the structure of aconitase, activated with  $\text{Fe}^{2+}$  and dithionite in the crystal, has been determined at 2.5 Å resolution.<sup>34</sup> Under these conditions,  $\text{Fe}^{2+}$  is inserted isomorphously in the  $[3\text{Fe}-4\text{S}]$  cluster, the fourth ligand to the  $[4\text{Fe}-4\text{S}]$  cluster is water (or hydroxyl) and the  $\text{SO}_4^{2-}$  remains bound.

At 2.1 Å resolution the electron density is consistent with four inorganic sulfurs in the core of the Fe-S cluster, as shown by the analysis of Fe:S ratios in inactive aconitase.<sup>14</sup> The presence of three cysteines as terminal ligands implies that one of the

inorganic sulfur atoms is trivalent. The Fe . . . Fe distances are 2.71, 2.64, 2.73 Å in agreement with the EXAFS results<sup>14</sup> and the 2.7 Å anomalous difference Patterson function.<sup>33</sup> The [3Fe-4S] structure from aconitase superposes within 0.09 Å, on average, on the [3Fe-4S] cluster in the 1.9 Å resolution structure of a 7Fe ferredoxin.<sup>54</sup> The geometry of the aconitase [3Fe-4S] cluster is also very similar to the [4Fe-4S] cluster in activated aconitase, except for the loss of one Fe,<sup>34</sup> and to the [3Fe-4S] cluster in *D. gigas* ferredoxin II.<sup>55</sup> Additional residues with atoms within 3.5 Å of the aconitase [3Fe-4S] cluster are I<sub>146</sub>, H<sub>148</sub>, H<sub>168</sub>, S<sub>358</sub>, I<sub>426</sub> (van der Waals contacts), and C<sub>359</sub> (o/c), and N<sub>447</sub> (possible NH . . . S hydrogen bonds). Hence, there are only two NH . . . S hydrogen bonds, compared to nine per [4Fe-4S] cluster in 8Fe ferredoxin.<sup>56</sup> The possibility for charged NH . . . S interactions from H<sub>102</sub>, H<sub>148</sub>, and H<sub>168</sub>, given small movements of these side chains.

### BOUND ANION

A large electron density peak not identifiable as any protein side chain is observed in the putative active site 9.3 Å from the center of the Fe-S cluster (Fig. 13d). This density has been modeled and refined as a SO<sub>4</sub><sup>2-</sup> ion for the following additional reasons: the crystals are grown from 2.2 M (NH<sub>4</sub>)<sub>2</sub>SO<sub>4</sub>; a peak comparable to other sulfur peaks is observed at the same site in the 3.0 Å Bijvoet difference Fourier map (Fig. 5b); recognizable density for the weak inhibitor tricarballoylate used in the crystallization is not found at the active site; the peak is flanked by the side chains of R<sub>581</sub> and R<sub>645</sub>, which would provide charge balance. All four oxygens of the SO<sub>4</sub><sup>2-</sup> in the model appear to be accepting hydrogen bonds from side chains: two from R<sub>645</sub> in bidentate fashion, two from R<sub>581</sub>, and one each from Q<sub>73</sub> and S<sub>644</sub>. Additional interactions are from the amide of R<sub>645</sub> and four water molecules. A sulfate ion is observed to bind in the active site of malate dehydrogenase in place of malate.<sup>49</sup> While the SO<sub>4</sub><sup>2-</sup> may be binding at a site where aconitase substrates bind, the significance of this to the mechanism cannot be inferred from this structure alone.

### REACTIVE CYSTEINE

Derivatization of a single reactive cysteine with phenacyl bromide blocks the activity of aconitase.<sup>57</sup> However, it has been shown that inactivation depends upon the size of the blocking group; small groups have no effect, but bulky groups such as *N*-ethylmaleimide completely inactivate the enzyme.<sup>58</sup> The sequence of the tryptic peptide containing this reactive cysteine has been determined,<sup>30</sup> in the structure it is C<sub>566</sub> (Fig. 13e). Surprisingly, this cysteine side chain is oriented inward to a cavity at the interface of the parallel  $\beta$ -sheet and  $\alpha$ -helices in domain 4 (Fig. 10c). The S $\gamma$  atom of C<sub>566</sub> is 20.3 Å from

the center of the Fe-S cluster in the crystal; a spin-labeling experiment indicated that the distance is approximately 12 Å.<sup>59</sup> The inactivation may work by an indirect mechanism since domain 4 is adjacent to the active site and the C $\alpha$  of 566 is next to the cleft. If the blocking group on the thiol is large enough, distortion or rotation of the chain at 566 would limit access to the active site via the cleft.<sup>58</sup>

### SUMMARY

The structure of aconitase reveals a four domain protein with a cleft leading to the Fe-S cluster at the active site. Originally, the three point hypothesis was proposed based on the stereoselectivity of the aconitase reaction.<sup>1-6</sup> The three N-terminal domains of the protein share a common folding motif and are tightly associated around the Fe-S cluster. The fourth domain is attached by a hinge-like peptide, creating a cleft with the first three domains. The arrangement of the four protein domains mimics the supposed 3-fold binding of substrate and the 3 plus 1 chemistry of the roles of Fe atoms in the reaction. There are three cysteine ligands to the [3Fe-4S] cluster, all provided by the third domain. The putative active site contains three histidines, in association with two asparates and a glutamate. The active site contains a bound sulfate ion which may mimic the binding of anionic substrates. The active site region does not contain a free cysteine in a position to rebuild a [4Fe-4S](S $\gamma$ )<sub>4</sub> cluster.

### ACKNOWLEDGMENTS

We wish to thank D. Aul and W.E. Brown for providing protein samples, H. Zalkin, J.B. Howard, and W.E. Brown for making available sequence data prior to publication, J. Hogle and I.A. Wilson for use of their laboratory during heavy atom derivative survey experiments, M. Pique and D.A. Case for computer graphics, and M.H. Emptage, J.B. Howard, H. Beinert, M.C. Kennedy, A.W. Schwabacher, D. Hilvert, and T. Poulos for helpful discussions. This work supported by NIH Grant GM-36325.

### REFERENCES

1. Ogston, A.G. Interpretation of experiments on metabolic processes, using isotopic tracer elements. *Nature (London)* 162:963 (1948).
2. Potter, V.R., and Heidelberger, C. Biosynthesis of "asymmetric" citric acid: A substantiation of the Ogston concept. *Nature (London)* 164:180-181 (1949).
3. Gawron, O., and Glaid, A.J. On the stereochemistry of the isocitric and allosocitric lactones. *J. Am. Chem. Soc.* 77: 6638-6640 (1955).
4. England, S. Configurational considerations in relation to the mechanisms of the stereospecific enzymatic hydrations of fumarate and *cis*-aconitate. *J. Biol. Chem.* 235:1510-1516 (1960).
5. Gawron, O., Gliad, A.J., III, and Fondy, T.P. Stereochemistry of Krebs' cycle hydration and related reactions. *J. Am. Chem. Soc.* 83:3634-3640 (1961).
6. Rose, I.A., and O'Connell, E.L. Mechanism of aconitase action. *J. Biol. Chem.* 242:1870-1879 (1967).

7. Villafranca, J.J., and Mildvan, A.S. The mechanism of aconitase action. *J. Biol. Chem.* 246:772-779 (1971).
8. Dickman, S.R., and Cloutier, A.A. Activation and stabilization of aconitase by ferrous ions. *Arch. Biochem.* 25:229-230 (1950).
9. Glusker, J.P. Mechanism of aconitase action deduced from crystallographic studies of its substrates. *J. Mol. Biol.* 38:149-162 (1968).
10. Carrell, H.L., Glusker, J.P., Villafranca, J.J., Mildvan, A.S., Dummel, R.J., and Kun, E. Fluorocitrate inhibition of aconitase: Relative configuration of inhibitory isomer by x-ray crystallography. *Science* 170:1412-1414 (1970).
11. Glusker, J.P. Aconitase. In "The Enzymes" (P.D. Boyer, Ed.). New York: Academic Press, 1971: Vol. 5, 413-439.
12. Kennedy, C., Rauner, R., and Gawron, O. On pig heart aconitase. *Biochem. Biophys. Res. Commun.* 47:740-745 (1972).
13. Ruzicka, F.J., and Beinert, H. The soluble "high potential" type iron-sulfur protein from mitochondria is aconitase. *J. Biol. Chem.* 253:2514-2517 (1978).
14. Beinert, H., Emptage, M.H., Dreyer, J.-L., Scott, R.A., Hahn, J.E., Hodgson, K.O., and Thomson, A.J. Iron-sulfur stoichiometry and structure of iron-sulfur clusters in three-iron proteins: Evidence for [3Fe-4S] clusters. *Proc. Natl. Acad. Sci. U.S.A.* 80:393-396 (1983).
15. Ryden, L., Overstedt, L.-G., Beinert, H., Emptage, M.H., and Kennedy, M.C. Molecular weight of beef heart aconitase and stoichiometry of the components of its iron-sulfur cluster. *J. Biol. Chem.* 259:3141-3144 (1984).
16. Beinert, H., and Thomson, A.J. Three-iron clusters in iron-sulfur proteins. *Arch. Biochem. Biophys.* 222:333-361 (1983).
17. Kent, T.A., Dreyer, J.-L., Kennedy, M.C., Huynh, B.H., Emptage, M.H., Beinert, H., and Münck, E. Mössbauer studies of beef heart aconitase: Evidence for facile interconversions of iron-sulfur clusters. *Proc. Natl. Acad. Sci. U.S.A.* 79:1096-1100 (1982).
18. Kennedy, M.C., Emptage, M.H., Dreyer, J.-L., and Beinert, H. The role of iron in the activation-inactivation of aconitase. *J. Biol. Chem.* 258:11098-11105 (1983).
19. Emptage, M.H., Dreyer, J.-L., Kennedy, M.C., and Beinert, H. Optical and EPR characterization of different species of active and inactive aconitase. *J. Biol. Chem.* 258:11106-11111 (1983).
20. Kennedy, M.C., Emptage, M.H., and Beinert, H. Incorporation of [<sup>35</sup>S]sulfide into the Fe-S cluster of aconitase. *J. Biol. Chem.* 259:3145-3151 (1984).
21. Emptage, M.H., Kent, T.A., Kennedy, M.C., Beinert, H., and Münck, E. Mössbauer and EPR studies of activated aconitase: Development of a localized valence state at a subsite of the [4Fe-4S] cluster on binding of citrate. *Proc. Natl. Acad. Sci. U.S.A.* 80:4674-4678 (1983).
22. Kent, T.A., Emptage, M.H., Merkle, H., Kennedy, M.C., Beinert, H., and Münck, E. Mössbauer studies of aconitase. *J. Biol. Chem.* 260:6871-6881 (1985).
23. Telser, J., Emptage, M.H., Merkle, H., Kennedy, M.C., Beinert, H., and Hoffman, B.M. <sup>17</sup>O electron nuclear double resonance characterization of substrate binding to the [4Fe-4S]<sup>1+</sup> cluster of reduced active aconitase. *J. Biol. Chem.* 261:4840-4846 (1986).
24. Kennedy, M.C., Werst, M., Telser, J., Emptage, M.H., Beinert, H., and Hoffman, B.M. Mode of substrate carboxyl binding to the [4Fe-4S]<sup>+</sup> cluster of reduced aconitase as studied by <sup>17</sup>O and <sup>13</sup>C electron-nuclear double resonance spectroscopy. *Proc. Natl. Acad. Sci. U.S.A.* 84:8854-8858 (1987).
25. Emptage, M.H. Aconitase: Evolution of the active-site picture. In: "ACS Symposium Series" (L. Que, Jr., Ed.), "Metal Clusters in Proteins," Vol. 372, pp. 343-371 (1988).
26. Schloss, J.V., Emptage, M.H., and Cleland, W.W. pH profiles and isotope effects for aconitases from *Saccharomyces lipolytica*, beef heart, and beef liver.  $\alpha$ -methyl-cis-aconitase and threo-D<sub>8</sub>- $\alpha$ -methylisocitrate as substrates. *Biochemistry* 23:4572-4580 (1984).
27. Schloss, J.V., Porter, D.J.T., Bright, H.J., and Cleland, W.W. Nitro analogues of citrate and isocitrate as transition-state analogues for aconitase. *Biochemistry* 19:2358-2362 (1980).
28. Hammershoi, A., Sargeson, A.M., and Steffen, W.L. Reactivity studies of chelated maleate ion: Stereoselectivity and structural correlations. *J. Am. Chem. Soc.* 106:2819-2837 (1984).
29. Gahan, L.R., Harrowfield, J.M., Herlt, A.J., Lindoy, L.F., Whimp, P.O., and Sargeson, A.M. Metal ion promoted hydration of pendant alkenes and its possible relationship to aconitase. *J. Am. Chem. Soc.* 107:6231-6242 (1985).
30. Plank, D.W., and Howard, J.B. Identification of the reactive sulfhydryl and sequences of cysteinyl-tryptic peptides from beef heart aconitase. *J. Biol. Chem.* 263:8184-8189 (1988).
31. Zalkin, H., private communication.
32. Aul, D., and Brown, W.E., private communication.
33. Robbins, A.H., and Stout, C.D. Iron-sulfur cluster in aconitase. *J. Biol. Chem.* 260:2328-2333 (1985).
34. Robbins, A.H., and Stout, C.D. Structure of aconitase: Formation of the [4Fe-4S] cluster in the crystal. *Proc. Natl. Acad. Sci. U.S.A.*, 86:3639-3643 (1989).
35. Robbins, A. H., Stout, C.D., Piszkiwicz, D., Gawron, O., Yoo, C.S., Wang, B.C., and Sax, M. Single crystals of the iron-sulfur enzyme aconitase. *J. Biol. Chem.* 257:9061-9063 (1982).
36. Kennedy, M.C., Kent, T.A., Emptage, M., Merkle, H., Beinert, H., and Münck, E. Evidence for the formation of a linear [3Fe-4S] cluster in partially unfolded aconitase. *J. Biol. Chem.* 259:14463-14471 (1984).
37. Xuong, Ng.H., Nielsen, C., Hamlin, R., and Anderson, D. *J. Appl. Crystallogr.* 18:342-350 (1985).
38. Hamlin, R. Multiwire area x-ray diffractometers. In: "Methods in Enzymology" (H.W. Wyckoff, C.H.W. Hirs, and S.N. Timasheff, eds.). New York: Academic Press, 1985: Vol. 114, 416-452.
39. Howard, A.J., Nielsen, C., and Xuong, N.G.H. Software for a diffractometer with multiwire area detector. In: "Methods in Enzymology" (H.W. Wyckoff, C.H.W. Hirs, and S.N. Timasheff, eds.). New York: Academic Press, 1985: Vol. 114, 452-471.
40. Terwilliger, T.C., Kim, S.H., and Eisenberg, D. Unbiased three-dimensional refinement of heavy-atom parameters by correlation of origin-removed Patterson functions. *Acta Crystallogr.* A39:813-817 (1983).
41. Wang, B.C. Resolution of phase ambiguity in macromolecular crystallography. In: "Methods in Enzymology" (H.W. Wyckoff, C.H.W. Hirs, and S.N. Timasheff, eds.). New York: Academic Press, 1985: Vol. 115, 90-112.
42. Strahs, G., and Kraut, J. Low-resolution electron-density and anomalous-scattering-density maps of *Chromatium* high-potential iron protein. *J. Mol. Biol.* 35:503-512 (1968).
43. Jones, T.A. A graphics model building and refinement system for macromolecules. *J. Appl. Crystallogr.* 11:268-272 (1978).
44. Sim, G. A. A note on the heavy atom method. *Acta Crystallogr.* 13:511-512 (1960).
45. Stuart, D., and Artymiuk, P. The use of phase combination in crystallographic refinement: The choice of amplitude coefficients in combined synthesis. *Acta Crystallogr.* A40:713-716 (1985).
46. Brünger, A. T., Karplus, M., and Petsko, G. A. Crystallographic refinement by simulated annealing: Application to crambin. *Acta Crystallogr.* A45:50-61 (1989).
47. Richardson, J.S. The anatomy and taxonomy of protein structure. *Adv. Prot. Chem.* 34:167-339 (1981).
48. Adams, M.J., Ford, G.C., Koekoek, R., Lentz, P.J., McPherson, A., Rossmann, M.G., Smiley, I.E., Schevitz, R.W., and Wonacott, A.J. Structure of lactate dehydrogenase at 2.8 Å resolution. *Nature (London)* 227:1098-1103 (1970).
49. Birktoft, J.J., and Banaszak, L.J. The presence of a histidine-aspartic acid pair in the active site of 2-hydroxyacid dehydrogenases. *J. Biol. Chem.* 258:472-482 (1983).
50. Karplus, P.A., and Schulz, G.E. Refined structure of glutathione reductase at 1.54 Å resolution. *J. Mol. Biol.* 195:701-729 (1987).
51. Donohue, J. Hydrogen bonded helical configurations of the polypeptide chain. *Proc. Natl. Acad. Sci. U.S.A.* 39:470-478 (1953).
52. Remington, S., Wiegand, G., and Huber, R. Crystallographic refinement and atomic models of two different forms of citrate synthase at 2.7 and 1.7 Å resolution. *J. Mol. Biol.* 158:111-152 (1982).
53. Kennedy, M.C., and Beinert, H. The state of cluster SH

- and  $S^{2-}$  of aconitase during cluster interconversions and removal. *J. Biol. Chem.* 263:8194–8198 (1988).
54. Stout, C.D. Refinement of the 7Fe ferredoxin from *Azotobacter vinelandii* at 1.9Å resolution. *J. Mol. Biol.* 205:545–555 (1989).
55. Kissinger, C.R., Adman, E.T., Sieker, L.C., and Jensen, L.H. Structure of the 3Fe–4S cluster in *Desulfovibrio gigas* ferredoxin II. *J. Am. Chem. Soc.* 110:8721–8723 (1988).
56. Adman, E., Watenpaugh, K.D., and Jensen, L.H. NH . . . S hydrogen bonds in *Peptococcus aerogenes* ferredoxin, *Clostridium pasteurianum* rebredoxin, and *Chromatium* high potential iron protein. *Proc. Natl. Acad. Sci. U.S.A.* 72:4854–4858 (1975).
57. Hahn, K.-S., Gawron, O., and Piszkievich, D. Amino acid sequence of a peptide containing an essential cysteine residue of pig heart aconitase. *Biochim. Biophys. Acta* 667: 457–461 (1981).
58. Kennedy, M.C., Spoto, G., Emptage, M.H., and Beinert, H. The active site sulfhydryl of aconitase is not required for catalytic activity. *J. Biol. Chem.* 263:8190–8193 (1988).
59. Dreyer, J.-L., Beinert, H., Keana, J.F.W., Hankovsky, O.H., Hideg, K., Eaton, S.S., and Eaton, G.R. A spin-label study of the disposition of the Fe-S cluster with respect to the active center of aconitase. *Biochim. Biophys. Acta* 745: 229–236 (1983).